

Predictive Understanding of Socioeconomic Flood Impact in Data-Scarce Regions Based on Channel Properties and Storm Characteristics: Application in High Mountain Asia (HMA)

Mariam Khanam^{1, 2}, Giulia Sofia¹, Wilmalis Rodriguez¹, Efthymios I. Nikolopoulos³, Binghao Lu⁴, Dongjin Song⁴ and Emmanouil N. Anagnostou¹

¹Civil & Environmental Engineering, University of Connecticut, Storrs, 06269, USA

²Water Resources Science and Engineering, Oak Ridge National Laboratory, Oak Ridge, 37771, USA

³Civil & Environmental Engineering, Rutgers University, Piscataway, 08854, USA

⁴Computer Science and Engineering, University of Connecticut, Storrs, 06269, USA

Correspondence to: Mariam Khanam (khanamm@ornl.gov), Giulia Sofia (giulia.sofia@uconn.edu)

Abstract. High Mountain Asia (HMA) faces heightened vulnerability to natural disasters due to its extreme conditions and the escalating impacts of climate change. Understanding the long-term response of this landscape to hydroclimatic fluctuations is imperative, given the profound effects these changes have on millions of people annually. Heavy rain and monsoon season bring forth floods and debris flows, resulting in significant damage to crops, infrastructure, and communities, causing widespread human impacts. Despite efforts to estimate flood risk locally, traditional techniques often fall short due to the scarcity of high-quality, consistent data, especially in ungauged basins. To overcome this challenge, we propose a novel approach: a geomorphologically guided machine learning (ML) method for mapping flood effects across HMA. Central to our methodology is the Lifyear Index (LYI), a systematic measure that quantifies both the financial and human losses incurred by disasters, specifically for this study, fluvial and pluvial flooding. Our model was trained using a dataset comprising over 6000 flood events spanning from 1980 to 2020, along with their corresponding five-year and ten-year LYI. Key predictors included: (1) five-year rainfall concentrations derived from ERA5 daily data, (2) a geomorphic classifier based on hydraulic scaling functions derived from high-resolution digital elevation models (DEM), and (3) population density. Results demonstrate the model's effectiveness in identifying flood susceptibility hotspots at a national scale and delineating their evolution from 1980 to 2020. Moreover, the study underscores the severity of hydroclimatic extremes across the entire HMA region. Importantly, the proposed framework is versatile and can be adapted to generate various pluvial and fluvial flood vulnerability and risk maps in ungauged regions.

29 High Mountain Asia (HMA) presents complex terrain characterized by dynamic hydrological and
30 geomorphological processes. Over recent years, the region has been significantly affected by climate change, notably
31 witnessing accelerated glacial melts (Shrestha and Aryal, 2011; Byers et al., 2022) and shifts in precipitation patterns and
32 intensity (Haag et al., 2019; Kirschbaum et al., 2020). These environmental changes, compounded by anthropogenic
33 influences such as landscape alterations, have escalated the region's susceptibility to flooding (Byers et al., 2022; Pervin et
34 al., 2020; Shrestha et al., 2010; Zheng, G. et al., 2021), with consequent increasing threats to lives, agriculture, and critical
35 infrastructure (Fischer et al., 2022; Pervin et al., 2020; Rentschler et al., 2022; Sharma et al., 2019; Torti, 2012). The direct
36 impacts caused by the flood are only part of the picture; the enduring socioeconomic repercussions further compound the
37 crisis. These include loss of livelihoods, the urgent need for rehabilitation efforts, and the psychological toll exacted on
38 affected communities.

39 Flood disasters are generally associated with hydroclimatic extremes. The variability of precipitation patterns over
40 time, space, and intensity is indeed crucial to their occurrence, but changes in catchment characteristics can also alter flood
41 magnitude and frequency. The complex geomorphology and orographic characteristics in the HMA region cause significant
42 spatiotemporal heterogeneity of precipitation patterns and extremes (Haag et al., 2019). Furthermore, the geomorphic
43 structure of basins in HMA can influence the flood characteristics more than land cover does (Marston et al., 1996). Many
44 floods in HMA carry huge amounts of sediment and water that adversely affect downstream areas where most population
45 resides and can remain in the landscape for years afterward (Kafle et al., 2017; Simonovic et al., 2022).

46 Changes in river morphology and channel shifting resulting from sediment variability are recognized causes of
47 flood risk (Blench, 1969; Criss & Shock, 2001; Lane et al., 2007; Neuhold et al., 2009; Pinter et al., 2008; Slater et al., 2015;
48 Stover & Montgomery, 2001; Sofia & Nikolopoulos, 2020a). Several researchers have highlighted how the morphometric
49 characteristics of watersheds provide useful insights into their hydrologic response to rainfall (Borga et al., 2008) since their
50 morphometric characteristics are a crucial influence on flash flood intensity. In HMA, however, these control mechanisms
51 are difficult to model at a large scale.

52 Accurate evaluation of the socioeconomic impacts of natural disasters is paramount to mitigate the sufferings of the
53 affected people and rehabilitation (Cavallo & Noy, 2010; Meyer et al., 2013; Noy, 2015, 2016a). To date, available studies
54 (Diehl et al., 2021; Mohanty & Simonovic, 2022; Pangali Sharma et al., 2019; Pervin et al., 2020; Piacentini et al., 2020;
55 Yang & Tsai, 2000) have primarily concentrated on vulnerability mapping and risk analysis, employing case studies and
56 descriptive event-based methodologies at a local level. Scaling up the analysis over the entire HMA region is indeed a
57 difficult task, as it requires collecting data from several countries and multiple sources, and this poses challenges due scarcity
58 of ground observations covering consistent timeframes homogeneously (Dollan et al., 2024; Miles et al., 2021). Especially in
59 the context of the impact of floods using socioeconomic data, the analysis involves examining the number of fatalities,
60 people injured, and otherwise affected, as well as the financial damage that natural disasters cause, and this information is

61 generally collected at the local scale based on reported events. Significant disasters are documented in global databases like
62 The International Disaster Database (EMDAT, www.emdat.be) or, as an example for HMA and this study, the Nepal
63 Disaster Risk Reduction Portal (<http://drrportal.gov.np/>). However, these databases typically operate at a global or national
64 level resolution, potentially overlooking minor disasters. For example, EMDAT only considers events with at least one of the
65 following criteria: 1) 10 fatalities; 2) 100 affected people; 3) a declaration of state of emergency; 4) a call for international
66 assistance. Additionally, those databases utilized to support insurance may prioritize countries with existing or potential
67 insurance coverage (World Bank, 2012).

68 The integration of geomorphic properties, population data, and rainfall characteristics for assessing socioeconomic
69 flood impact is only recently being explored comprehensively on a large scale (e.g., Janizadeh et al., 2024). For HMA, this is
70 primarily due to the inherent challenges associated with conducting on-site surveys in rugged and often inaccessible terrain.
71 However, leveraging remote sensing data has emerged as a valuable approach for delving deeper into these dynamics and
72 effectively quantifying flood impacts. Modern global datasets, featuring improved resolution and coverage, further enhance
73 the utility of remote sensing in this regard (Diehl et al., 2021; Jongejan & Maaskant, 2015; Mosavi et al., 2018; Bentivoglio
74 et al., 2022; Mazzoleni et al., 2022; Hawker et al., 2018; Kirschbaum et al., 2020; Mohanty and Simonovic, 2022; Pangali
75 Sharma et al., 2019; Sanyal and Lu, 2004; Yang and Tsai, 2000; Zheng et al., 2018).

76 Furthermore, machine learning (ML) techniques have emerged as increasingly popular tools in advanced prediction
77 systems over the past two decades. They offer more cost-effective solutions with performance that can be aggregated,
78 surpassing the complexity and time demands associated with simulating the complex development of flood processes.
79 Recent research (Bentivoglio et al., 2022; Deroliya et al., 2022; Mosavi et al., 2018) has showcased encouraging
80 advancements by integrating machine learning (ML) techniques with global datasets. This contemporary approach to
81 mapping flood vulnerability notably streamlines the computational processes associated with data-intensive simulations,
82 enhancing flood risk management strategies. However, ML systems rely on existing data for learning. Insufficient or
83 incomplete data coverage can hinder effective learning, leading to suboptimal performance when deployed in real-world
84 scenarios. Therefore, ensuring robust data enrichment, encompassing both quantity and quality, is imperative.

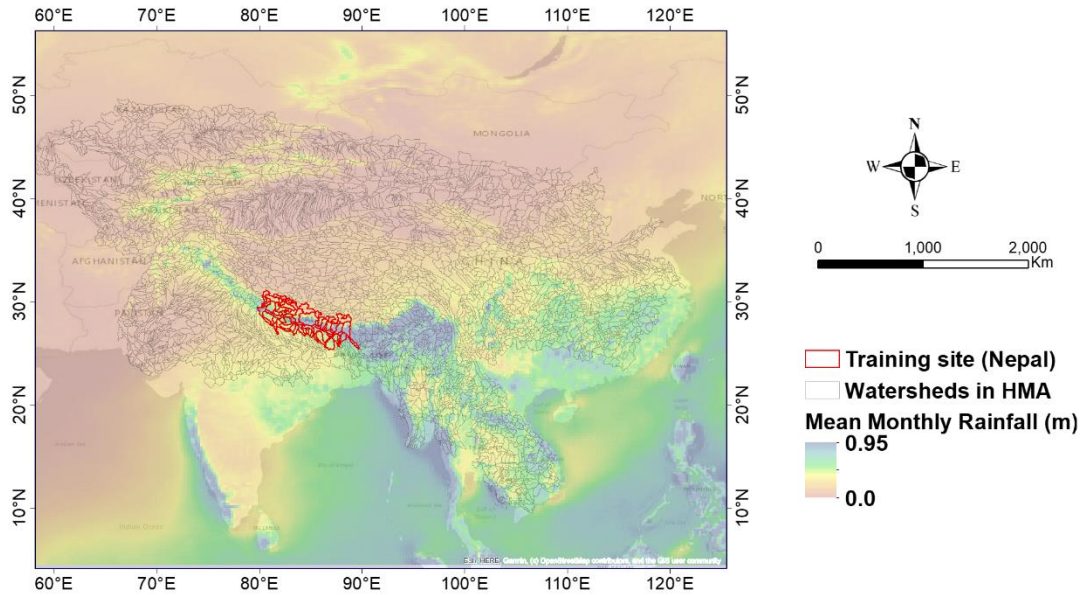
85 In this study, we introduce a streamlined methodology for preliminary flood vulnerability assessment on a large
86 scale, leveraging available global datasets. Specifically, we introduce a flood-risk assessment model designed to quantify
87 spatially distributed socioeconomic susceptibility in flood-prone regions. We utilize this model to augment disaster
88 understanding by integrating remotely sensed data, including climate variables and high-resolution terrain information.
89 Finally, we apply this model in the High Mountain Asia (HMA) regions to analyze changes in socioeconomic flood impacts
90 spanning from 1980 to 2020.

91 2 Materials and Methods

92 2.1 Study Area

93 HMA, otherwise known as the Hindu Kush-Himalayan region, comprises Nepal, Pakistan, Bangladesh, Bhutan,
94 India, Afghanistan, Kazakhstan, Kyrgyzstan, Tajikistan, Uzbekistan, Mongolia, China, and part of many other countries in
95 Asia. HMA is home to some of the world's highest mountain systems, including the Himalayas and the Hindu Kush. This
96 rugged terrain has a highly variable climate ranging from tropical to subpolar, essentially controlled by altitude. Around 1.5
97 billion people (<https://nsidc.org/data/highmountainasia>) dwelling in the region are at risk of natural disasters (such as heavy
98 rainfall, flooding (pluvial/ fluvial/ flash), earthquakes, avalanches, and landslides) due to the topographic characteristics,
99 changing climate patterns, and high population density. Some of the world's largest rivers and deltas, such as the Indus and
100 the Ganges, are located in this region. In the summertime (June to September), monsoon rains bring a vast amount of water
101 (Kayastha & Kayastha, 2019) to the rivers and valleys in the southern part of HMA (Northern India, Nepal, Bangladesh, and
102 Pakistan). Kirschbaum et al. (2020) have projected that the greatest increase in very high intensities of precipitation (>20
103 mm/day) will occur during the monsoon season, with the enormous amount of rain causing all types of devastating floods
104 (Talchabhadel et al., 2018). Referring to the data reported, for example, in EMDAT, among all other hydroclimatic disasters
105 in HMA from 1980 to 2020, floods affected the most people (53% among all other hydroclimatic disasters) and caused the
106 highest total damage (56% among all other hydroclimatic disasters). Bangladesh, Nepal, Pakistan, and parts of India were
107 hotspots with the highest casualties (source: EMDAT).

108 This study considers approximately 6,000 watersheds across HMA as the main target area (Figure 1): the
109 watersheds were selected to be consistent with the HMA domain and all the datasets produced throughout the different
110 phases of the NASA-funded HiMAT project (<https://himat.org/>). The analysis initially centred on training and testing a
111 machine-learning model specifically for Nepal. To achieve this, we collected fine-resolution topographic data along with
112 district-scale socioeconomic information on population characteristics and documented flood impacts for this region.
113 Subsequently, leveraging the insights gained from this initial phase, we extended the application of the trained model to
114 predict socioeconomic impacts across all watersheds in HMA.



115

116 **Figure 1: Study area- watersheds across High Mountain Asia (HMA), with highlighted the training domain (Nepal) and the overall**
 117 **rainfall variability across the region. The watershed displayed in black represents the 6000 watersheds that were used in the study.**
 118 **The watersheds were selected to be consistent with the HMA domain and all the datasets produced throughout the different**
 119 **phases of the NASA-funded HiMAT project (<https://himat.org/>)**

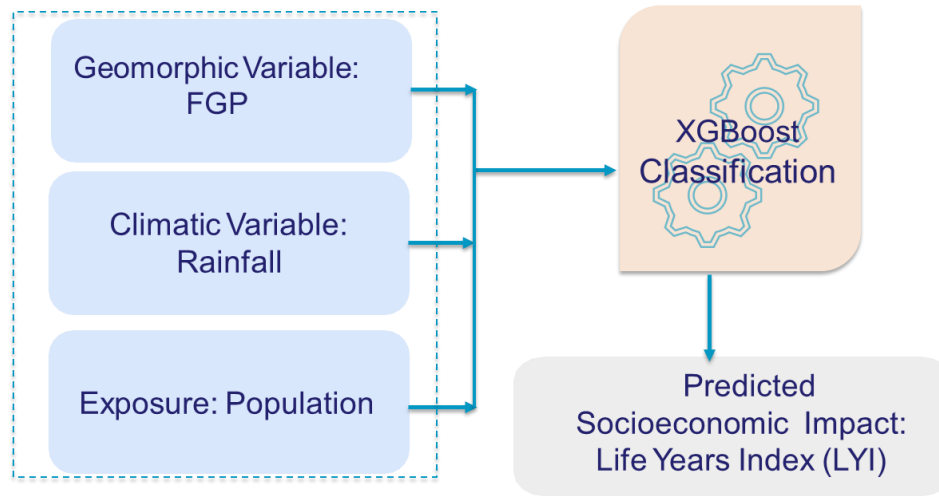
120 **2.2 Methods**

121 Figure 2 illustrates the conceptual framework guiding this study. We employed machine learning (ML) analysis,
 122 utilizing climatic and geomorphologic variables, to forecast the socioeconomic impact of extreme fluvial and pluvial flood
 123 events spanning from 1980 to 2020 across High Mountain Asia (HMA). To capture the link between flooding and climatic
 124 and geomorphologic processes, the model considers as predictors a climatic index derived from ERA5 rainfall, and a
 125 geomorphological index, the Flood Geomorphic Potential -FGP- that characterizes the flood-proneness of the landscape,
 126 together with population data. A notable advantage of the proposed approach lies in its reliance on automatic techniques
 127 leveraging globally available datasets, thereby facilitating its applicability across diverse geographical regions to forecast
 128 socioeconomic flood impacts. The framework also benefits from leveraging geomorphologically driven information to have
 129 an improved characterization of the different aspects of the underlying physical processes shaping the landscape and possibly
 130 impacting flood characteristics. By incorporating such domain knowledge into the ML model, the framework can better
 131 generalize across different regions and conditions, improving robustness and reliability for risk mapping in diverse
 132 environments and facilitating informed decision-making for flood management and mitigation strategies.

133

134 To represent exposure and socioeconomic impacts, we introduced, respectively, a variable for population and
 135 “Lifeyears Index” (LYI) (Noy, 2014, 2016a, 2016b), a unit of measurement used to describe a disaster’s impact in terms of

136 the total years of life lost (see section 2.3.1 for details). To predict the LYI, we applied XGBoosting (eXtreme Gradient
137 Boosting) (Chen et al., 2018; Chen & Guestrin, 2016). The predictor and response variables of the ML framework are
138 described in the subsections below.



139
140 **Figure 2: Conceptual framework.** Considered predictors are Flood Geomorphic Potential (FGP), Rainfall, and Population. The
141 predicted value is the socioeconomic impact, characterized as the Lifeyears Index (LYI) (Noy, 2016a; Noy, 2015). Readers should
142 refer to the following sections for an explanation of the predictors and predicted values.

143 The analysis follows a multistep approach, beginning with data at both watershed and district scales. Initially, the
144 focus was on the district scale, as socioeconomic data for Nepal, selected as the primary training ground, were readily
145 available at this level through the Nepal Disaster Risk Reduction Portal (<http://drrportal.gov.np/>). For this region,
146 furthermore, there is a comprehensive coverage of high-resolution (8-meter) Digital Elevation Models (DEMs) from prior
147 High Mountain Asia (HMA) work (High Mountain Asia 8-meter DEMs Derived from Along-track Optical Imagery,
148 10.5067/0MCWJJH5ABYO). Subsequently, all the information is aggregated at the watershed scale, as phenomena such as
149 fluvial and pluvial flooding occur at this level, necessitating a dataset tailored to this scale.

150 To transfer the demographic information from the district to the watershed scale, we performed a weighted spatial
151 join between the watersheds and districts. For each watershed, we attributed the statistical characteristics of the intersecting
152 districts, with weights based on the overlapping areas. The aggregation from district to watershed is done by a weighted
153 average, considering the extent of the district area within the watershed as a weight. Generally, the districts in Nepal are
154 smaller in extent compared to the various watersheds.

155

156 2.3 Datasets

157 2.3.1. Socioeconomic Flood Impacts

158 The research focused on predicting the socioeconomic impact of floods. Measured economic loss and tangible
159 damages were analyzed by considering the Lifeyears Index (LYI) (Noy, 2014, 2016a, 2016b). This index is presented by

160 Noy (2016) as “Lifeyears lost” and it is a variant of the WHO Disability Adjusted Life Years (DALYs) lost due to diseases
 161 and injuries (WHO, 2014). We calculated LYI for Nepal by using damage statistics and demographic information collected
 162 from different data portals in Nepal.

163

164 The Index is described by Equation 1 and the parameters used in the equation are described in Table 1:

165

$$166 \quad LYI = M(A_{exp} - A_{med}) + e * T * N + (1 - c)Y/PCGDP \quad (1)$$

167

168 **Table 1: Parameters used to calculate LYI**

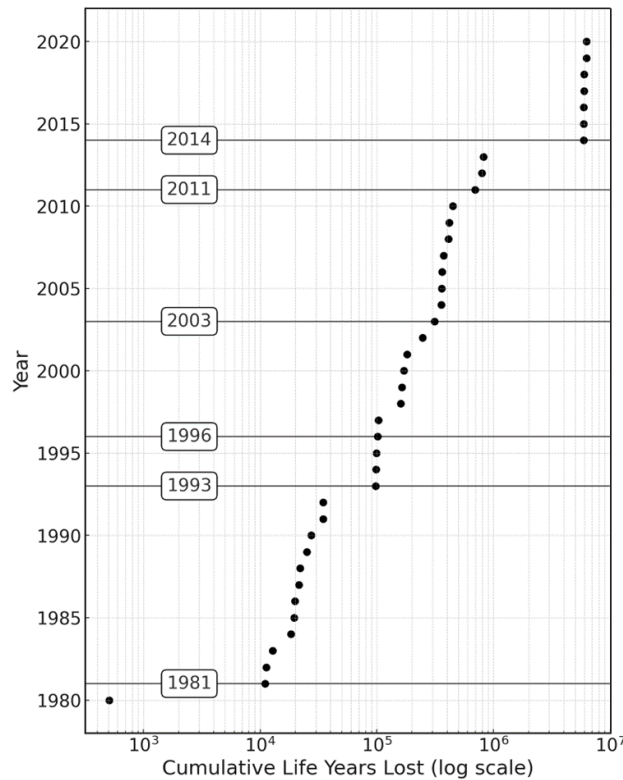
Variable	Description	References
		Nepal Disaster Risk Reduction Portal
M	Mortality (number of deaths due to disaster)	(http://drrportal.gov.np/)
A _{exp}	Average life expectancy at birth (by year)	WHO (https://data.who.int/countries/524)
A _{med}	Median age (by year)	WHO (https://data.who.int/countries/524)
e	Welfare reduction weight associated with being exposed to a disaster	set to e = 0.054 according to Noy, (2016a), based on Mathers et al., 2013
T	Time taken by the affected person to get back to normal	Noy, (2016a)
N	Number of affected people	Nepal Disaster Risk Reduction Portal (http://drrportal.gov.np/)
c	Percent of time not used in work-related activities (.75)	Noy, (2016a)
Y	Financial damage (value of destroyed/damaged infrastructure)	Nepal Disaster Risk Reduction Portal (http://drrportal.gov.np/)
PCGDP	Income per capita (by year)	The World Bank (https://data.worldbank.org/country/Nepal)

169

170 In this study, we classified Lifeyears Index (LYI) values into three distinct categories: Low for cases where
 171 $\log(LYI) < 2$; Medium for values falling between 2 and 3; and High for $\log(LYI) > 3$. This classification scheme indicates
 172 that a watershed or district is deemed to be at high risk if the average LYI exceeds 1000 years, while medium risk spans LYI
 173 values ranging from 100 to 1000 years, and Low risk encompasses LYI values less than 100 years. For instance, if the

174 calculated LYI is 100 years, it implies that the estimated impact of the given disaster equates to a potential loss of 100 years
175 of life per 100,000 people.

176 The cumulative LYI for Nepal (Figure 3) can provide an idea of how the cumulated flood impact has been
177 increasing in a country with time. It also highlights how the index itself captures major disasters, such as those occurring in
178 1981 (ICIMOD, 2011; Kiran S et al., 2008), 1993 (Nepal - Floods and Landslides, 1993), in 1996 (Nepal - Floods Situation
179 Report No. 1, 26 July 1996), and in the monsoon seasons in 2003 and 2014 (Nepal Annual Report, 2003.; Nepal: Landslides
180 and Floods - Aug 2014). The most changes can be noticed in the LYI for the years 1981, 1993, and 2014, the cumulative
181 step change for these years from the previous year are subsequently 9999, 82865, and 976238 years.



182

183 **Figure 3: Cumulative lifeyears lost over the years in Nepal. Highlighted years represent jumps in the cumulative value, mostly**
184 **related to well-known disasters): 1981 (ICIMOD, 2011; Kiran S et al., 2008), 1993 (Nepal - Floods and Landslides, 1993), 1996**
185 **(Nepal - Floods Situation Report No. 1, 26 July 1996), and in the monsoon seasons in 2003 and 2014 (Nepal Annual Report, 2003.;**
186 **Nepal: Landslides and Floods - Aug 2014).**

187 2.3.2. Floodplain Mapping

188 The identification of areas with the potential to be inundated is fundamental to preserving and protecting human
189 lives and property while safely supporting economic activities. Hence, we applied a large-scale floodplain delineation
190 algorithm to identify such areas at the basin scale across the HMA. Many researchers (e.g., Dingle et al., 2020; Lindersson et
191 al., 2021; Piacentini et al., 2020; Sofia, 2020b) have used DEM-derived geomorphic indices as a high-resolution flood

192 mapping tool. We opted for considering a variation of the Samela et al. (2017), which is a modified Geomorphic Flood Index
193 (GFI) by Sofia et al., 2017 & Sofia et al., 2015, thereby described as Flood Geomorphic Potential (FGP).

$$194 \quad \text{FGP} = \ln (h_r / H) \quad (2)$$

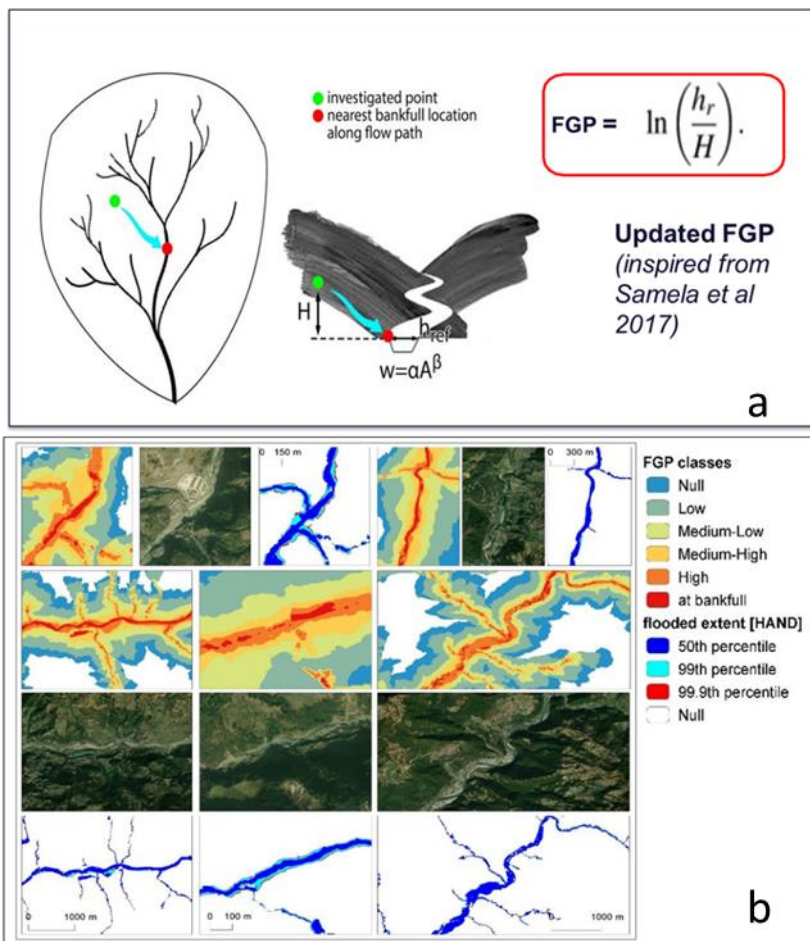
195 The index is calculated as the logarithm function of the bankfull elevations, H (estimated using a hydraulic scaling
196 function, or HSF ($w=\alpha A^\beta$), based on bankfull width (w) and contributing area (A)) in the element of the river network closest
197 to the point under examination and the elevation difference between these two points, h_r (Figure 4, Equation 2). The index
198 was improved over a main aspect: the automatic identification of the HSF directly from terrain data, applying the technique
199 of Sofia et al., 2017 & Sofia et al., 2015 to retrieve the bankfull location automatically through the landscape. This has the
200 advantage of allowing for full automation of the mapping starting purely from terrain data.

201 For this analysis, we trained the model considering FGP derived from the unique 8-meter Digital Elevation Models
202 (DEMs) for Nepal that are available at the NASA National Snow and Ice Data Center Distributed Active Archive Center
203 (NSIDC DAAC) (Shean, 2017). While Nepal is entirely covered by the 8m DEM, extending the model to the whole HMA
204 region is complicated by the gaps in the input satellite strip resulting from limited coverage, clouds, or failed stereo
205 correlation. For this reason, we also considered the 30m DEM by Copernicus (European Space Agency, Sinergise.
206 Copernicus Global Digital Elevation Model, 2021), a digital surface model (DSM) that represents the surface of the Earth,
207 including buildings, infrastructure, and vegetation. Importantly, this DSM is derived from World DEM, an edited DSM in
208 which the flattening of water bodies and the consistent flow of rivers have been included. Shore and coastlines, special
209 features such as airports, and implausible terrain structures have also been edited.

210 We identified flood-prone areas by grouping them into six classes by their FGP index. For each watershed, we then
211 considered the areas covered by the classes with FGP greater than 4, which, when compared to published data, proved to
212 correspond realistically with areas subject to floods of about 100-year depth. Figure 4b compares the Flood Geomorphic
213 Potential (FGP) automatic classes derived for select rivers in Nepal, with baseline inundation scenarios evaluated using
214 standard inundation depths associated with critical flood events and their return periods provided in the work of Delalay et
215 al. (2018). This visual comparison serves to highlight the efficacy of flood inundation mapping facilitated by the FGP. The
216 HAND (Height Above Nearest Drainage) in Delalay et al. (2018) is a widely used approach for estimating flood inundation
217 extents and water depths. It operates on the principle of deriving relative elevations from a DEM, similar to our approach,
218 which also relies on DEM-based analysis. While having assumptions may introduce some limitations in accurately capturing
219 complex flood dynamics, HAND remains a useful and practical method for large-scale flood assessment due to its
220 computational efficiency and compatibility with readily available topographic data. Given these similarities, we find it
221 reasonable to include HAND as a comparative reference in our study while acknowledging its limitations.

222 It's worth noting that the DEM-derived geomorphic index has been previously published and applied in various
223 contexts (Samela et al., 2017). While testing the quality of the DEM-derived geomorphic index lies beyond the scope of this
224 work, its effectiveness for flood mapping has been well-established in previous studies (e.g. Manfreda & Samela, 2019),
225 which have demonstrated the utility of the methodology, particularly in ungauged conditions, for preliminary identification

226 of flooded areas in regions where conducting expensive and time-consuming hydrologic-hydraulic simulations may not be
 227 feasible.



228
 229 **Figure 4: a. Flood Geomorphic Potential (FGP) (modified from Samela et al. 2017); b. FGP automatic classes compared to baseline**
 230 **inundation depth (HAND) scenarios and Orthophotos of selected areas (aerial imagery © Google Earth 2015).**

231 2.3.3. Rainfall Characteristic

232 The climatology in HMA is highly variable (Dollan et al. 2024). Summer monsoons drive precipitation in the
 233 Ganges-Brahmaputra basins and the Tibetan Plateau (Bookhagen and Burbank, 2010; Shamsudduha and Panda, 2019);
 234 synoptic storms dominate winter precipitation, impacting areas in the northwestern Karakorum mountains (Winiger et al.,
 235 2005; Barlow et al., 2005). Overall, as well, variations in elevation gradients contribute to diverse microclimates,
 236 exemplified by Nepal's swift transition from high mountains to lowlands (Kansakar et al., 2004; Karki et al., 2016). Winter
 237 precipitation in the area is primarily influenced by the westerly weather system, with western disturbances originating in the
 238 Mid-Atlantic or Mediterranean Sea and traversing through northwest India to western Nepal after passing over Afghanistan

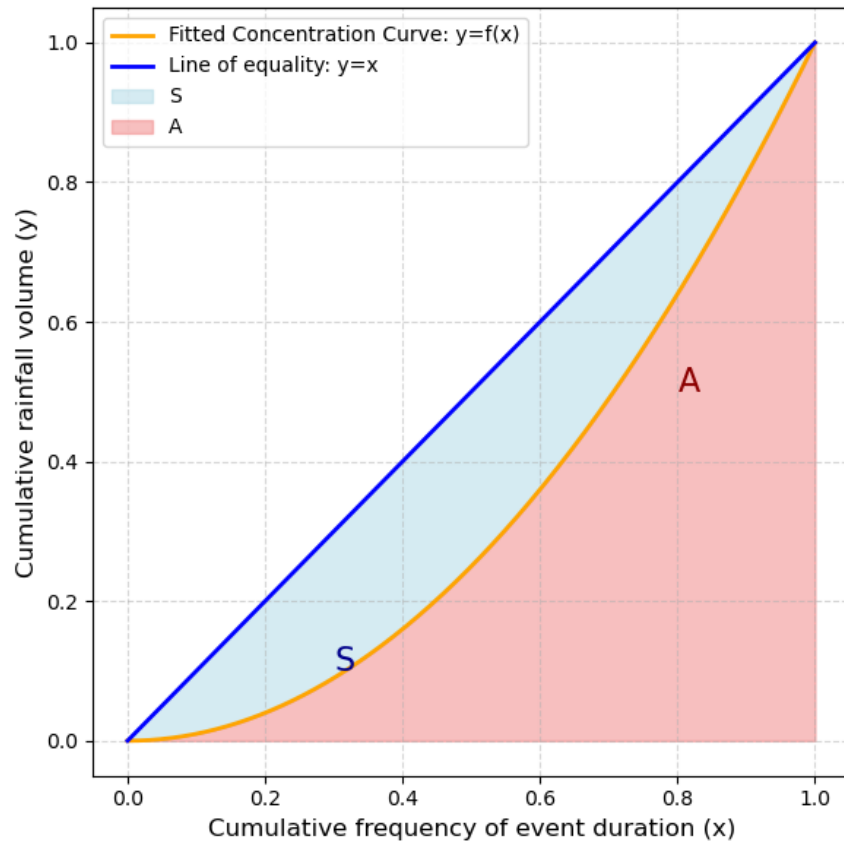
239 and Pakistan (Kansakar et al., 2004; Hamal et al., 2020). In Nepal, which was used as the training site for the model, regional
240 climate variations exist, mostly driven by changes in elevation, with an overall homogeneity in trends (aside from a few
241 hotspots) and regional statistics of precipitation, in line with the variability of HMA, as highlighted by the recent study by
242 (Khanal et al., 2023).

243 For this work, for the main rainfall driver of the model, we focused on daily climate concentration. As climate
244 concentration values are mostly related to the temporal variability of the rainfall, not to the total amount or the average
245 yearly and seasonal statistics, using this index allows us to capture various climates globally (Monjo and Martin-Vide, 2016).
246 The variability of climate concentration, furthermore, has been proven to be highly linked to pluvial/fluviial flooding impacts
247 in various regions of the world, including for example Italy (both in mountainous landscapes and floodplains (Sofia et al.,
248 2019), the US (Saki et al., 2023) [over a variety of physiographic regions], or China (Du et al., 2023). Different authors have
249 adopted different methods to determine the temporal concentration of precipitation, and the Concentration Index (CI)
250 (Equation 2) is one of the most used parameters (Caloiero et al., 2019; Martin-Vide, 2004; Monjo, 2016; Sangüesa et al.,
251 2018; Serrano-Notivoli et al., 2018).

$$252 \quad CI = \frac{S}{S+A} \quad (2)$$

253 This index was proposed by Martin-Vide (2004) originally to explore the contribution of the days with major
254 rainfall to the total amount within a certain time range. The benefit of this index is that it can describe the temporal
255 variability of rainfall at daily, annual, and seasonal scales using a single metric, as well as spatial variability at pixel or
256 watershed scale. In the present study, we computed CI (Martin-Vide, 2004) using the ERA5 hourly rainfall data from 1980
257 to 2019. The source of rainfall data was selected as various works for HMA highlighted its effectiveness in capturing
258 extreme events quite accurately compared to other products (Maggioni & Massari, 2018; Maina et al., 2023; Dollan et al.,
259 2024). The CI was calculated considering a 5-year window. The choice of this length was made to have sufficient data to
260 calculate the index, as well as to be able to capture variability over the 49 years of this analysis.

261 We identified storm events from this dataset primarily based on the criterion of rainfall of more than 0.5 mm, and
262 we separated events when rainfall was below this threshold for more than 12 hours. Furthermore, we calculated CI using the
263 cumulative amount of rainfall and the cumulative frequency of the event duration (Figure 5) for the selected events. The
264 method (similar to Cortesi et al., 2012 and Monjo & Martin-Vide, 2016) eventually aggregates the amount of precipitation
265 that falls during each event into increasing categories and determines the relative contribution (as a percentage) of the
266 progressively accumulated precipitation, as a function of the accumulated percentage of the durations of the events. The
267 concentration index is then calculated as the ratio of the area between the line of equality ($y=x$) and the fitted curve (S), and
268 the total area under the line of equality ($A+S$) (Figure 5, equation 2). The index is defined by the relationship between the
269 accumulated percentage of time, and the accumulated rainfall.



270

271 **Figure 5: Example of the line of equality and empirical curve for the rainfall concentration calculation. The concentration index is**
 272 **equal to the area between the line of equality and the fitted curve (S) divided by the total area below the line of equality (S+A)**

273 2.3.4. Exposure (Population)

274 As all the parameters of the LYI are not always readily available at the watershed scale (as highlighted by most
 275 published literature, which considered LYI at the country scale), we added population counts as one of the predictors to train
 276 the model. For Nepal, we selected the data from the country's national census
 277 (<https://censusnepal.cbs.gov.np/Home/Index/EN>) and aggregated it at the watershed scale by using the previously mentioned
 278 weighted join. To extend the model to the whole HMA, we computed the population for each watershed across the region
 279 from the Gridded Population of the World (GPW), v4 | SEDAC, 2024). This dataset provides spatially explicit estimates of
 280 population density for the years 2000, 2005, 2010, 2015, and 2020, based on counts consistent with national censuses and
 281 population registers, as raster data to facilitate data integration. We used a simple linear regression to retrieve data for the
 282 missing years.

283 2.4. Machine Learning Model

284 XGBoosting is primarily used to solve classification problems. To generate the results, the XGBoost algorithm uses
 285 an ensemble of boosted trees. An ensemble is a collection of predictors that together can give a final prediction while

286 reducing errors significantly. In this case, the predictors were climatic variables, geomorphologic variables, and exposure.
287 Boosted algorithms are those in which each successive model attempts to correct the errors of its predecessor (similar to
288 adaptive learning). The basic XGBoost algorithm can be understood as an ensemble of boosted trees. The idea behind such
289 an ensemble is that multiple trees are built in sequence, each tree built on the previous one's prediction. And each successive
290 tree built considers the errors of the previous trees. This means that when we take an average of all the trees at the end, we
291 get a final tree that is better than any individual tree within the model. We applied the XGBoosting model to the
292 geomorphologic, climatic, and exposure variables to predict classes of LYI in different basins in Nepal and HMA.

293 **2.4.1 Validation of the System at the HMA Scale**

294 We conducted thorough testing and validation of our model for Nepal, comparing the predicted value of LYI to the
295 calculated Lifyears Index (LYI) data from tabular values specific to the region. We trained the model and validated it only
296 using the data for Nepal, at the district scale and then at the watershed scale. Overall, we opted for a 90-10 approach, for
297 which 90% of the Nepal data were used for training and 10% for validation. Upon extending the model's applicability to the
298 entire High Mountain Asia (HMA) region, we rigorously assessed the quality of our results by comparing the predicted
299 social impact with that reported in established flood databases covering the region. We performed a hyperparameter tuning
300 using weighted accuracy (1-3-9 weighting scheme) for subsequently (low, med, and high classes), prioritizing category
301 "high". Initially, when XGBoost was trained, it achieved a 63% test accuracy, but its confusion matrix revealed that it
302 struggled to correctly classify the most destructive category (category 3). Since this category was of primary interest, the
303 model was refined using weighted accuracy, emphasizing its importance. A 5-fold cross-validation with 1000 iterations was
304 conducted, and for each cross-validation, oversampling was applied to balance the dataset.

305 To verify our findings, we compared the predictions at the HMA level with flood events reported in the Dartmouth
306 Flood Observatory's (DFO) Global Active Archive of Large Flood Events, 1985–Present. This comprehensive database
307 compiles information on major floods sourced from diverse channels such as news reports, governmental records, ground
308 observations, and remote sensing data. Notably, the DFO dataset encompasses various flood types, including lowland floods
309 and mountainous river floods characterized as fluvial and pluvial floods. The dataset provides point locations, representing
310 the centroids of affected areas during floods. While acknowledging that flood centroids may oversimplify the complexities
311 driving flood events, we utilized this dataset to showcase our model's capability to target high-risk locations historically
312 impacted by floods within the specified timeframe. Identifying high-risk areas with recorded flood occurrences centered
313 around these locations underscores the robustness of the model beyond the confines of its training and validation site in
314 Nepal.

315 Meteorological and climatological severity reported in the DFO database does not directly reflect the social impact
316 of floods, and the events listed often span multiple watersheds. To address these limitations, we compared our model's
317 predictions to the DFO data using a proxy for social severity—specifically, the reported number of people affected,
318 including "Deaths" and "Displaced." Instead of relying on meteorological classifications, we grouped the DFO events by

319 social severity classes defined as 10^n , where n corresponds to the severity level indicated in the DFO database. We then
320 evaluated the marginal probability that events with varying DFO severity occurred in watersheds with different predicted
321 LYI (Local Yield Impact) levels. Additionally, we computed the conditional probability—that is, the likelihood of a DFO-
322 classified event occurring within watersheds predicted by our model to have a certain LYI classification. This conditional
323 probability helps assess how well our system identifies high-impact regions across different time frames. For example, if
324 only 10% of watersheds are classified as high impact by our model, but most of the DFO’s most severe events (e.g., those
325 with >1000 people affected) occurred within these watersheds, this would indicate that our model effectively captures
326 regions of elevated social risk. A more detailed discussion of model performance and validation is provided in Section 3.3.
327 Results Analysis

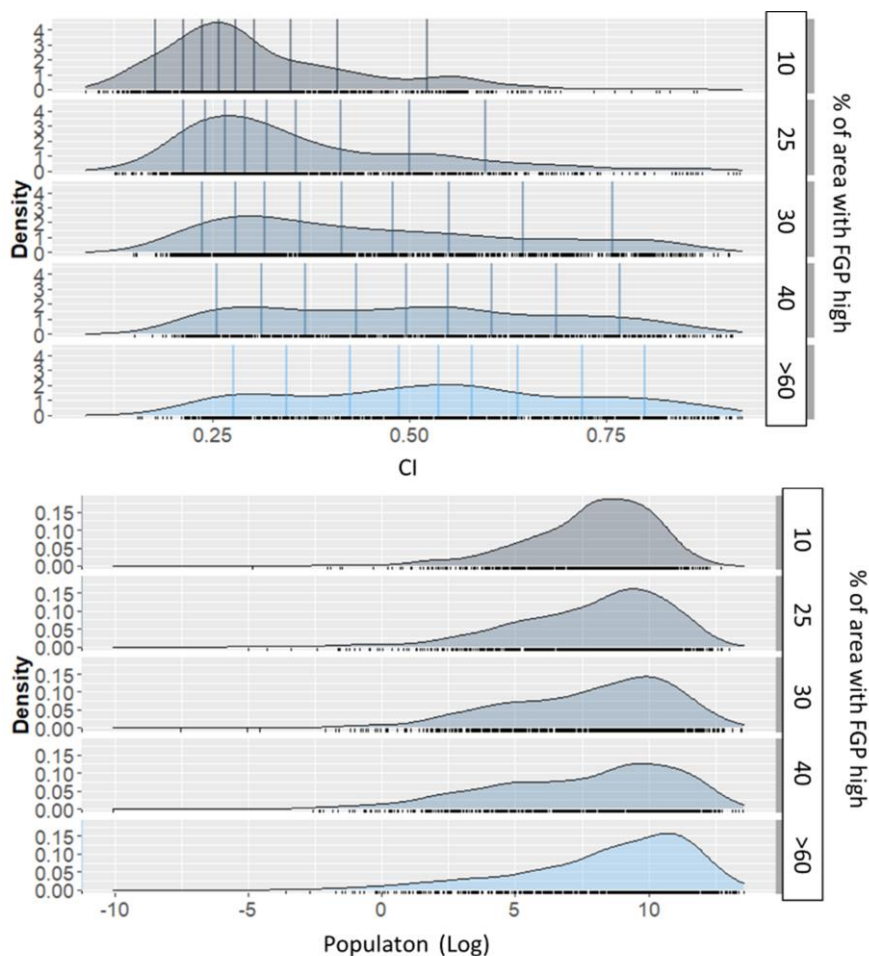
328 **3.1. Variability of the Predictors**

329 The topographical characteristics of an area can influence the local climate and population distribution. Figure 6
330 shows an example of how climate concentration and population vary in Nepal, as compared to watersheds that have areas of
331 high FGP to a greater or lesser extent. The figure reports the average for the time frame 1980–2020 for CI and population,
332 while the FGP is a static value for the time frame (since it is based on a unique DEM dataset), and it represents the overall
333 geomorphic characteristics of Nepal.

334 From this analysis, we can see how the variability of CI is complex. If expectedly, the variability of the index is
335 related to atmospheric characteristics (Sangüesa et al., 2018), the index also varies due to geographical factors influencing
336 climate (Tuladhar et al., 2020). In their study based on Nepal, Karki et al. (2017) highlighted the difference in the spatial
337 pattern of high-intensity storm events from that of annual and monsoon events. The rapid rate at which physical processes
338 (e.g., convection) take place regulates the high temporal concentration of precipitation in the regions where the sea surface
339 and ground are highly affected by warmer temperatures (Monjo & Martin-Vide, 2016). On the other hand, the low temporal
340 concentration of rainfall is characterized as a normal pattern caused by cyclical weather events (Monjo & Martin-Vide,
341 2016). Watersheds with lesser floodplain extents (that is, less areas with high FGP) are related to higher and steeper
342 mountains, with complex orography. Research has shown that low areas in Nepal are susceptible to receiving high-intensity
343 storm events even though they have fewer wet days (Karki et al., 2017). The authors of the same study also observed that the
344 low-intensity events (annual and monsoonal precipitation) were mostly predominant over Nepal’s western middle mountains
345 and central high mountains. In another study, however, Subba et al. (2019) stated that the frequency of extreme events had
346 decreased significantly over the past two decades in the eastern part of Nepal. For our case, areas having the larger physical
347 potential to flood (high FGP), appear to be areas showing the largest variation in CI, with values ranging from low (0.2) as
348 well as very high (0.75), indicating a potential compound effect of highly torrential rains (CI=0.7) in locations where much
349 of the landscape is potentially floodable (FGP high) and most population reside. Readers should consider that higher FGP

350 values do not imply locations having wider channels, but rather they indicate how the landscape is potentially more flood
351 prone as highlighted by (Samela et al., 2017; Manfreda & Samela, 2019).

352



353

354 **Figure 6: Average variability of the CI (top) and population (bottom) compared to FGP from 1980-2020**

355 Much of the population of Nepal tends to be concentrated in areas with higher FGP, as is typical for mountainous
356 areas, where population and economic activities are mostly located in the river valleys. Globally, the floodplains of rivers are
357 preferred living spaces for the population and provide favourable locations for economic development. These areas are
358 commonly exposed to floods, however, an increasing population, together with the changes in storminess, means that the
359 risks from flooding are expected to be higher. On average, the population increased significantly in watersheds that
360 transitioned from low to medium (LtoM), medium to high (MtoH), or low to high (LtoH) flood risk categories (Figure 7:
361 example variability from 1985 to 2020). This suggests that growing population density in certain watersheds may be
362 contributing to increasing flood susceptibility. The CI (climate concentration index) slightly decreased over this period for

363 some watersheds. However, watersheds experiencing population growth were more likely to influence the transition to a
 364 higher flood risk category. Although CI has not significantly increased, the interaction between land-use change, urban
 365 expansion, and demographic shifts may be playing a role in driving these transitions. Transitioning watersheds have a higher
 366 average FGP compared to the overall average FGP and tend to have a larger average watershed area compared to all
 367 watersheds. This indicates that larger watersheds are more prone to experiencing shifts in FGP and flood risk categories,
 368 possibly due to their ability to accumulate and distribute larger volumes of runoff and sediment. This supports the idea that
 369 intrinsic watershed characteristics (such as geomorphology and size) play a role in flood susceptibility alongside external
 370 factors like population growth and rainfall concentration index (CI). Area successfully predicted as at high risk (high LYI) in
 371 the most recent years, are areas showing high social vulnerability in terms of favorable Social Conditions (lack of
 372 communication, access to electricity and infrastructures, lower education, small children under 5); high percentage of
 373 migrating community and high risk of poverty and poor infrastructures (Aksha et al., 2019).
 374

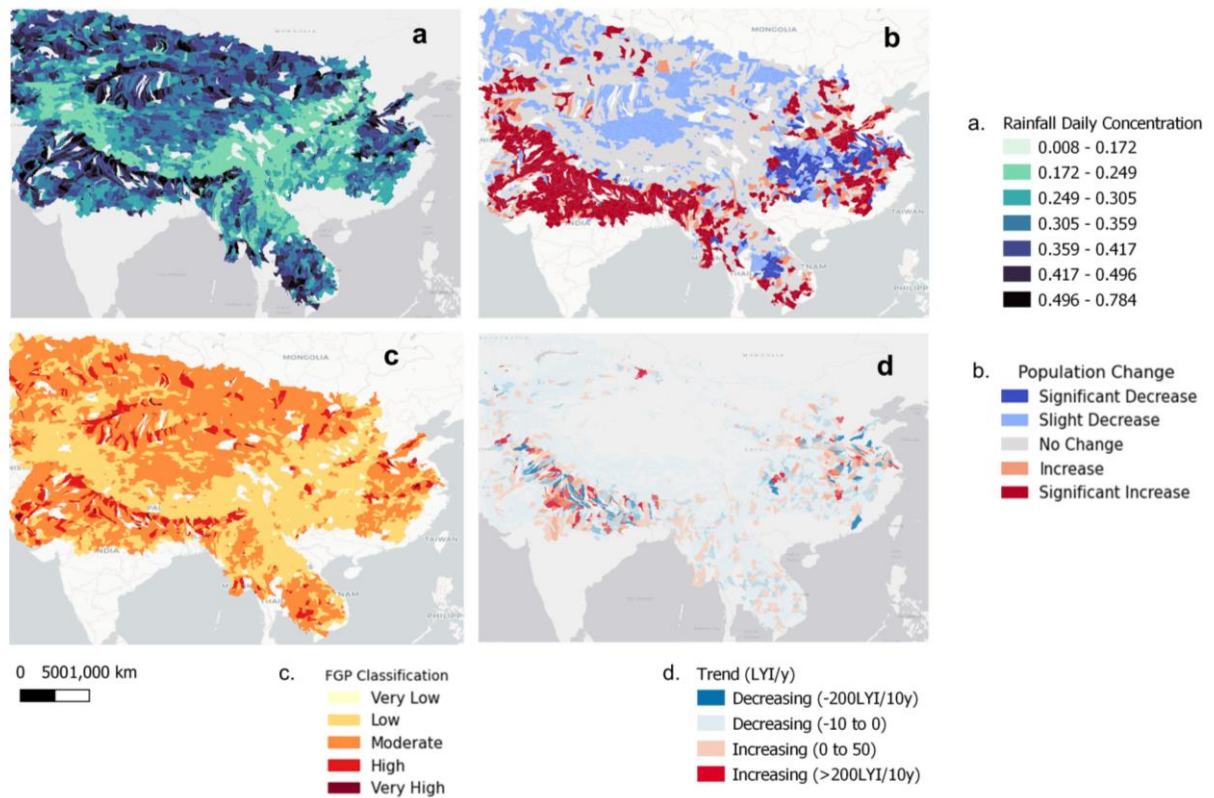


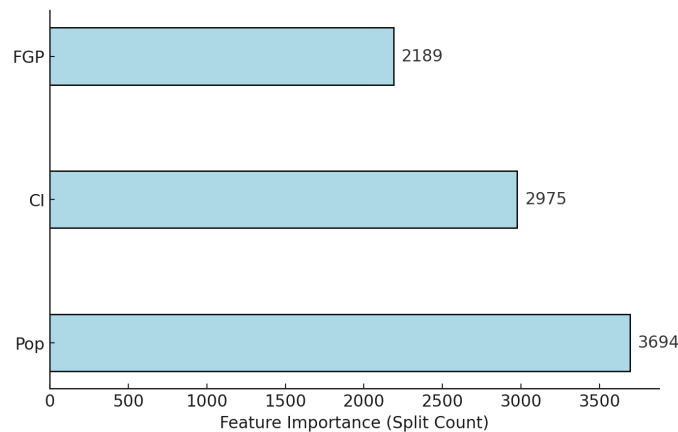
Figure 7: Average variability of the rainfall CI (a), population change (b), compared to FGP (c) and LYI Trend (d) from 1980-2020

379 3.2. Variable Importance and Model Performance

380 In this section, we present a variable importance comparison (Figure 8) based on the Feature Importance Score (F-
381 score) in XGBoost. XGBoost provides an F-score based on how frequently a feature is used in splitting the data across all
382 decision trees. This is the number of times a feature appears in a split across all trees in the model. A higher value indicates
383 that the feature was used more frequently in decision-making, suggesting it has a stronger influence on model predictions.
384 The F-score indicated that population (Pop) was the most important variable, which was consistent with our expectation in
385 the sense that the socioeconomic impact depends largely on the exposure. The climate variable (CI) happened to be the next
386 important variable, showing the significance of the region’s climate on the socioeconomic impact of flood occurrences.

387 The precision, recall, and F1 score are metrics used to evaluate the performance of a classification model. Precision
388 is the fraction of true positives among the predicted positives. Recall is the fraction of true positives among the actual
389 positives. The F1 score is the harmonic mean of precision and recall.

390 The evaluation metrics reveal in Table 2 that the model performs best in the High class, with the highest precision,
391 recall, and F1 score. The final tuned models achieved weighted accuracies between 52% and 58%, but significantly
392 improved recall (71%), precision (73%), and F1-score (72%) for category “high”. This means that out of 34 actual instances
393 of the highest category, 24 were correctly predicted, and out of 33 predicted cases, 24 were accurate, confirming that the
394 model effectively focused on the most critical category. This suggests that while the overall accuracy slightly decreased due
395 to the re-weighting, the model's performance in identifying the most critical cases significantly improved. The Medium class
396 also demonstrates relatively high performance across these metrics. However, the Low class exhibits the lowest
397 performance, suggesting that the model may face challenges in accurately distinguishing between the Low and Medium
398 classes or may demonstrate a bias toward predicting the Medium and High classes. These findings provide valuable insights
399 into the strengths and limitations of the classification model and can guide future efforts to improve its performance. Overall,
400 considering that the model aims to target substantial risk areas, a higher rate of predicting impacts is acceptable, compared to
401 an underestimation of the risk.



402
403 **Figure 8: Feature importance score (F-score)**

404 **Table 2: Performance metrics of the model on the test dataset**

	precision	recall	f1-score
Low	0.54	0.57	0.56
Medium	0.64	0.63	0.64
High	0.73	0.71	0.72

405

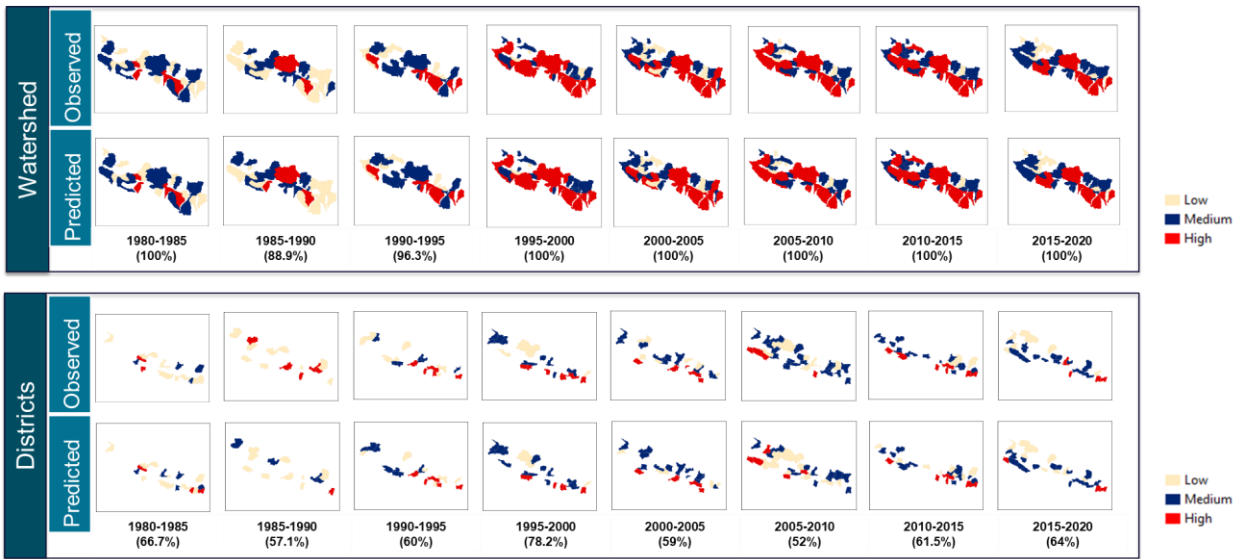
406 **3.3. Predicted versus Observed Flood Impact in Nepal**

407 Comparing predicted Lifyears Index (LYI) flood impacts with observed data showed good correspondence
408 between high-risk areas identified by the ML method and historical flood locations in Nepal. This suggests that the proposed
409 approach effectively delineates flood risk on a national scale. Figure 9 illustrates this comparison, showcasing observed
410 (empirically evaluated) and ML-predicted LYI values at both watershed (upper row) and district (lower row) levels.

411 The 'observed' LYI values were empirically calculated from observational data (Table 1) and categorized into three
412 groups: 'low', 'medium', or 'high', with basins/districts labelled as 'high' for LYI values exceeding 1000 years, 'medium'
413 between 100 and 1000 years, and 'low' below 10 years. The 'predicted' values represent the outputs from the machine
414 learning model.

415 In Nepal, we achieved an overall training accuracy of 97% and a test accuracy of 63%. Notably, training the model
416 at the watershed level yielded higher accuracy compared to the district level. This is attributed to watersheds being
417 hydrologic units that integrate geomorphological and climatic properties, thus providing a more accurate representation of
418 flood dynamics compared to administrative district boundaries.

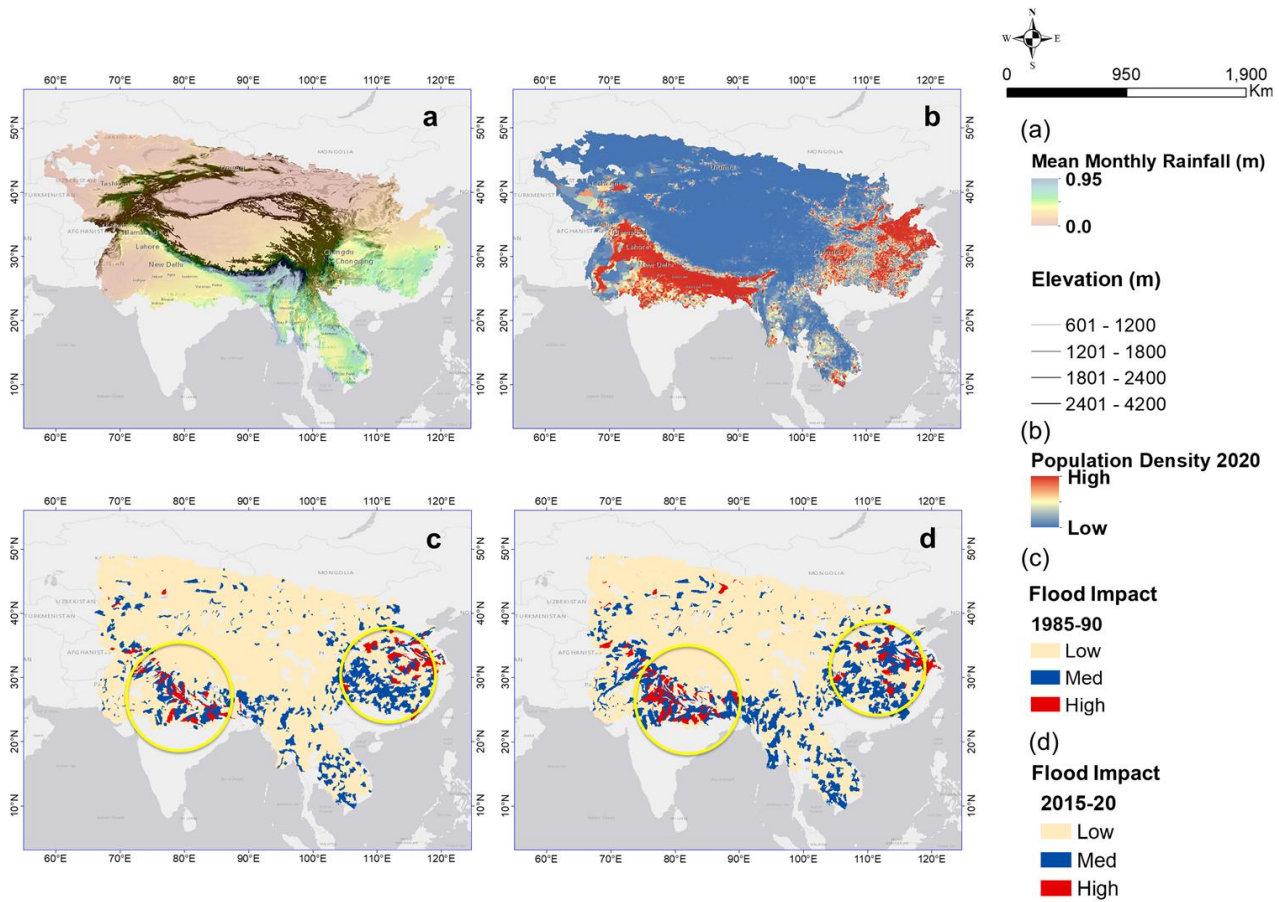
419 At the watershed level, nearly all year ranges exhibited a 100% match with observed impacts. In instances where
420 the model's accuracy fell below 100% (e.g., 1985–90 and 1990–95), the LYI values in the affected watersheds were low,
421 indicating that the predictors considered were more indicative of major flooding events. The superior accuracy achieved at
422 the watershed level underscores the value of implementing the model at this scale when scaling up the system.



423
424 **Figure 9: Comparison of prediction with actual socioeconomic impact for watersheds and districts in Nepal. Basin/districts are**
425 **marked as “high” for LYI over 1000 years. Medium is between 100 and 1000, and low is less than 10. Numbers in parentheses**
426 **represent accuracy.**

427 3.4. Prediction of Socioeconomic Impact of Heavy Rainfall over HMA

428 We applied the trained model for the watersheds in HMA to five-year intervals from 1980 to 2020. As an example,
429 Figure 10(c, d) shows the predicted basin-averaged LYIs (Low-Med-High) for the watersheds in HMA for two different
430 timelines. The yellow circles highlight the changes in flood impact over the decades. One must consider that most HMA
431 have low population density (blue color in Fig. 10 b), and as expected, the proposed model predicts low flood socioeconomic
432 impacts for these regions. Hotspots of high impacts (Red colors in Figures 10c and d) are present, where population exposure
433 is higher.



434

435 **Figure 10: a) Mean Monthly Rainfall overlaid on Elevation (contours); b) Population density 2020; c,d) Example of predicted**
 436 **basin-averaged flood impact for HMA (left, 1985–90; right, 2015–20). Yellow circles denote the changes in flood impact between**
 437 **the two timelines.**

438

439 Summarizing the results presented in Table 3, we can say that, for the years shown, we predicted almost 57% of
 440 watersheds (marginal) having LYIs between 1 and 100 years (Low), 35.9% for LYIs between 100 and 1000 years (Med),
 441 and only 6% for LYIs greater than 1000 years (High). For the entire period, most of the time we predicted LYIs of 1 to 100
 442 years, for which we captured events of DFO severity around 2 (10^2 Deaths + displaced) (conditional = 28.6%). This suggests
 443 that most “Low” class DFO events did happen in the watersheds within the lowest predicted LYI range. Readers must
 444 consider that “Low” in this case means the flood impact can range from 1 to 100 years lost, and a DFO value of 2 means
 445 total deaths and displaced is on the order of 10^2 people. The events with a DFO value of 4 happened mostly in watersheds
 446 with predicted LYIs ranging between 1 and 100 years and between 100 and 1000 years. The events with DFO 6 and 8
 447 happened mostly in ranges greater than 1000 years and between 100 and 1000 years.

447

448

DFO	LYI	NO	Prop	Marginal Probability	Conditional Probability
2	1–100yr	54	16.6	58.2	28.6
2	100–1000yr	26	8.0	35.7	22.4
2	>1000year	5	1.5	6.2	25.0
4	1–100yr	92	28.3	58.2	48.7
4	100–1000yr	45	13.8	35.7	38.8
4	>1000year	5	1.5	6.2	25.0
6	1–100yr	42	12.9	58.2	22.2
6	100–1000yr	44	13.5	35.7	37.9
6	>1000year	8	2.5	6.2	40.0
8	1–100yr	1	0.3	58.2	0.5
8	100–1000yr	1	0.3	35.7	0.9
8	>1000year	2	0.6	6.2	10.0

450

451 We further investigated how our predicted LYI behaved when it was related to the total population (Table 4),
452 evaluating, as suggested by (Noy, 2014), the LYI per capita (that is, the number of lifeyears lost per 100k people). As Table
453 4 shows, we correctly predicted over the years almost 64% of watersheds (marginal) have LYI/100k people less than 1 year
454 (10^0), 24.3% at 10year/100k people (10^1), 11% at 100year/100k people, and 0.6% at 1000years/100k people. We noticed
455 that LYI/100k people reached, at most, 6000 for Nepal (at the country scale), and the study by Noy. 2016a also reported
456 similar values for Nepal in 1987. (Noy, 2016a) reported actual LYI data in the range of LYI > 1000/100k people in South
457 Asia and stated that the higher number of damages in East and South Asia is likely due to wide-scale flooding. This gave
458 assurance of the consistency of our prediction with the actual data available. When looking at LYI/100k people, we found
459 that, for the whole timeframe, most of the floods that registered in the DFO with low severity (DFO = 10^2
460 Deaths+displaced) happened in watersheds for which the predicted LYIs were between 1 and 100 years (conditional =
461 29.8%). This confirmed once again that, in most cases, “low”-risk events did happen in the watersheds having the lowest
462 predicted range (similar to the findings presented in Table 3). As before, while the probability of a watershed’s being labeled
463 as high risk (LYI>1000year/1000k people) by our system was only 6%, the probability of these watersheds having
464 experienced events recorded by the DFO as having a great impact (DFO severity > 6, meaning over 1 million people) rose to
465 40% and 10%.

466

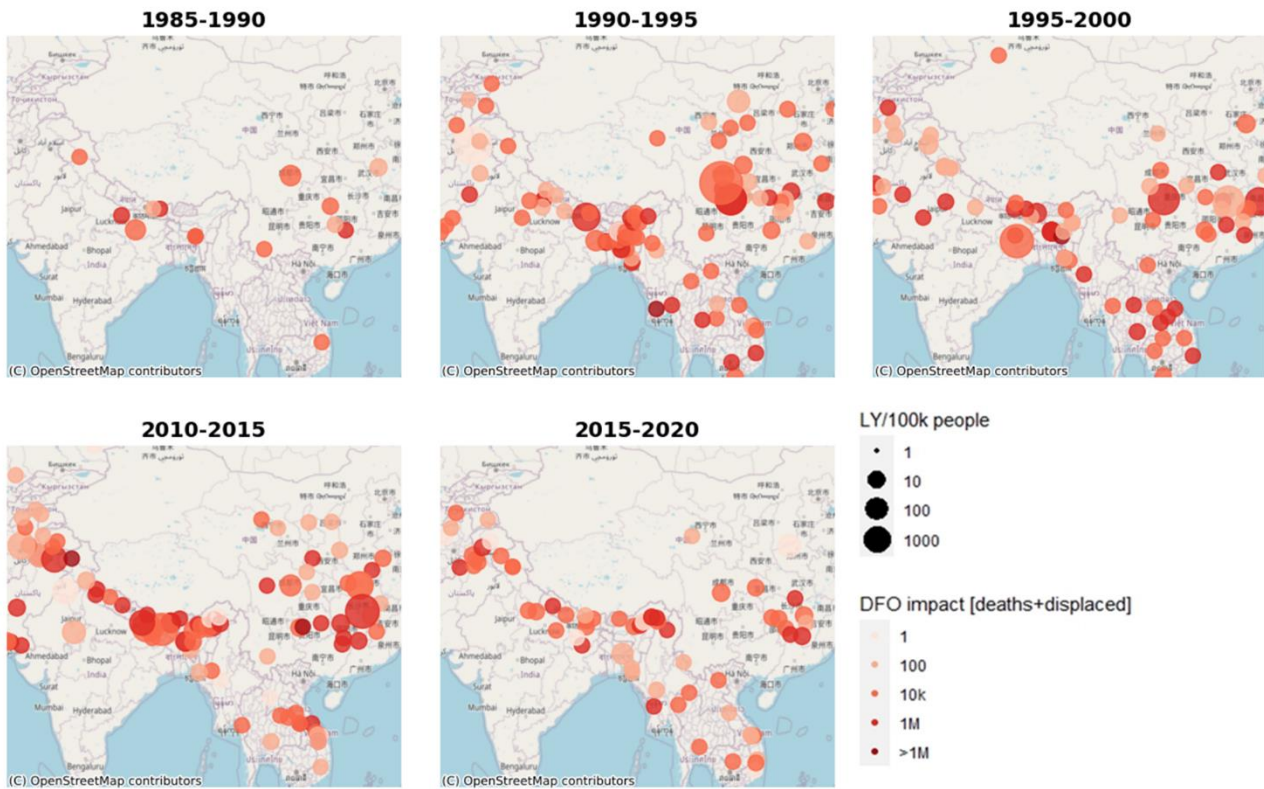
467

469 **Table 4: LYI/100k compared to DFO flood damage.**

DFO	LYI	NO	Prop	Marginal Probability	Conditional Probability
0	0	13	3.8	65.0	5.9
0	1	1	0.3	23.5	1.3
0	2	1	0.3	10.9	2.7
2	0	62	18.2	65.0	28.1
2	1	13	3.8	23.5	16.3
2	2	9	2.6	10.9	24.3
2	3	1	0.3	0.6	50.0
4	0	97	28.5	65.0	43.9
4	1	34	10.0	23.5	42.5
4	2	10	2.9	10.9	27.0
4	3	1	0.3	0.6	50.0
6	0	47	13.8	65.0	21.3
6	1	32	9.4	23.5	40.0
6	2	15	4.4	10.9	40.5
8	0	2	0.6	65.0	0.9
8	2	2	0.6	10.9	5.4

470

471 Figure 11 shows the LYI per 100k people (LYI/100k) evaluated for different time frames for all the locations
472 reported in the DFO database to compare the DFO severity with our predictions. Overall, the DFO and predicted results were
473 quite consistent instead with some minor variability in some scattered areas. When we compared the changes over time, we
474 noticed an increase in vulnerability. As the plot makes evident, the largest changes took place in 1990–95 and 2010–15; the
475 two concentrated areas were Nepal and China. As Figure 3 shows, two big jumps occurred during these timelines for Nepal
476 because of extreme storm-induced flood events. In Figure 3, we have discussed the predominant events that occurred in these
477 timelines. Regarding China, as of June 2010, more than 29 million people had been affected by flooding, with up to 2.37
478 million evacuated and 195,000 homes destroyed (China: Floods Information Bulletin N° 1 GLIDE N°, 2010).

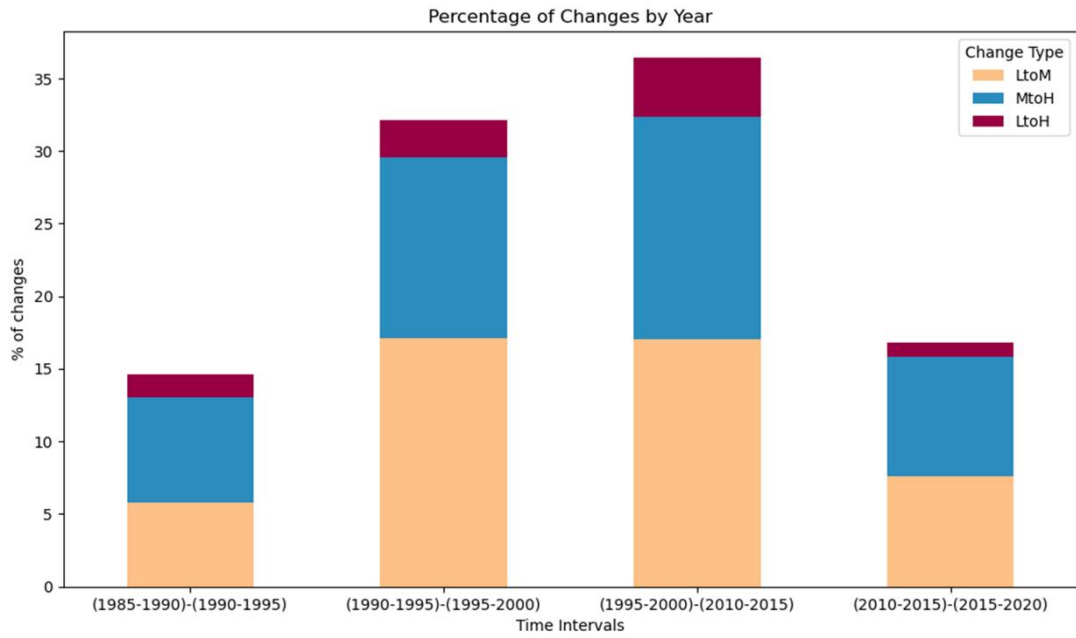
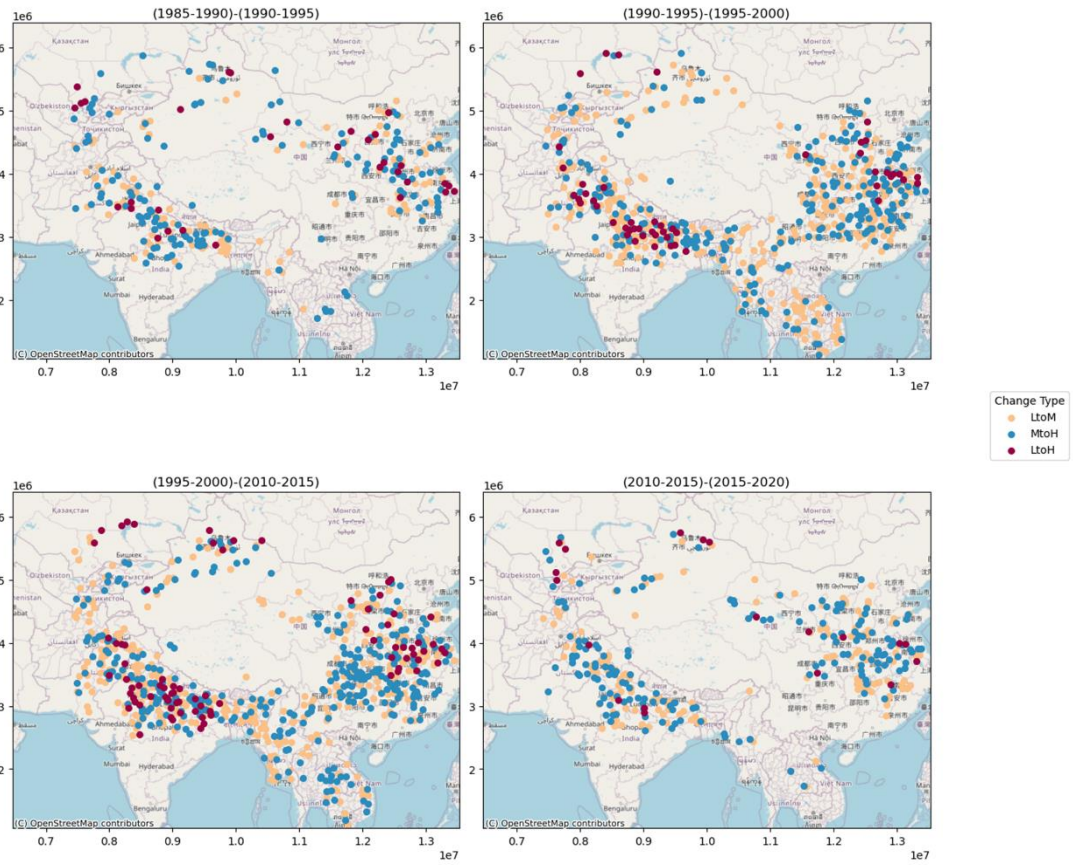


479
480 **Figure 11: Comparison of DFO and LYI/ 100K people for all the timelines**

481 **3.6. Change in Socioeconomic Impact over Time**

482 Figure 12a presents our maps of the watersheds where flood impacts increased over time. Furthermore, Figure 12b
483 shows our evaluation of the percentage changes in the number of watersheds between timelines, focusing on three different
484 changes: low to medium (LtoM); medium to high (MtoH); and low to high (LtoH). Some watersheds have not changed, and
485 some have decreased impact. For the sake of highlighting potential increases in flood impacts, we focused on those locations
486 where risk increased over time, from low to medium, or medium to high. The largest changes were from LtoM for all the
487 timelines, which represented a notable change in vulnerability. Several watersheds showed higher flood impacts (from low to
488 medium, medium to high, and low to high) in recent years as compared to 1985–90. Again, we observed the largest changes
489 for 1990–95 and 2010–15, which was consistent with Figure 12. The exposure changed significantly, along with the intensity
490 of the events; hence, the risk of flooding was heightened in these areas.

491 Impact changes from Low to High were next, according to the number of watersheds changed for all the timelines.
492 It was obvious that more changes would happen overall, but the comparison of the 1990–95 and 1995–2000 timelines
493 demonstrated that heightened flood impact occurred in a considerable number of watersheds within a brief period. For many
494 watersheds, the risk was heightened by a population boom during the overall period.



495

496 **Figure 12: Flood impact change in HMA over time**

497 **3.7. Model constraints and limits**

498 While this study demonstrates the promise of accurate flood impact prediction, the use of static Flood Geomorphic Potential
499 (FGP) maps presents limitations. Flooding alters channel morphology and downstream topography, impacting future flood dynamics
500 (Khanam et al., 2024). Therefore, dynamic flood topographies are essential for robust hazard assessment. Although high-resolution data
501 post-extreme events can enhance prediction accuracy, the availability of such data is constrained by acquisition frequency. Hence, efforts
502 to improve data availability post-disaster are crucial for enhancing the reliability of predictive models. Researchers could also derive FGPs
503 from enhanced high-resolution terrain data, such as that derived from LiDAR sources, if available. In such cases, however, it is advisable
504 to retrain the model and reassess the significance of this parameter in the updated model, as terrain resolution and survey techniques might
505 determine a variability of the data, especially when dealing with hydrologic parameters (Sofia, 2020a).

506 The climate index considered in this study might vary depending on the input dataset (Reanalysis VS measurements), as well as
507 on the timescale of the analysis. When comparing results to this study, researchers should make careful consideration of the length of the
508 time window used for this evaluation (5 years). If daily data are considered over shorter time windows (e.g., 1 year), the index itself might
509 result in higher values, capturing only short-term variability due to specific isolated storms. Seasonal analyses, on the other hand, would
510 capture more of the concentration due to monsoon periods, or dry vs. wet months. The proposed multi-year analysis is in line with
511 literature studies on climate change and on the effect of flooding (Sofia et al., 2019; Saki et al., 2023; Du et al., 2023).

512 Population data for this work relies on standard available datasets. When considering the method to predict future changes,
513 outside the time range covered by the proposed model, headcounts alone cannot offer a full picture. It is also crucial to consider additional
514 elements that could determine population shifts over time.

515 **4. Conclusions**

516 High Mountain Asia (HMA) presents a multifaceted landscape characterized by rugged terrain, diverse climates,
517 rich vegetation, and substantial population exposure to natural disasters. Given its susceptibility to natural disasters, effective
518 management is imperative for the region's long-term sustainability. Addressing the considerable threat posed by flooding
519 demands a comprehensive strategy involving disaster risk reduction, sustainable land use practices, and climate change
520 mitigation.

521 In this study, we introduced a simplified approach to identify vulnerability hotspots within the HMA region,
522 focusing on intense rainfall events. To map the socioeconomic flood vulnerability, we employed a remotely sensed data-
523 driven model integrating geomorphological and climate variability factors. This adaptable framework can be tailored to
524 various regions, provided that similar terrain and climate datasets are available, accommodating adjustments to flood drivers
525 such as climate and geomorphology, as well as population dynamics. The resulting predictions offer valuable insights into
526 vulnerabilities across HMA watersheds, facilitating proactive flood management planning.

527 The novelty of our study lies in the efficiency and versatility of the proposed predictive model. Requiring only a
528 small number of variables, our model accurately forecasts the socioeconomic impact of pluvial and fluvial flooding events.
529 In densely populated, possibly ungaged regions with rapidly changing climates, such a model serves as a valuable decision-

530 making tool for stakeholders. The efficacy of the framework, as demonstrated in Nepal, underscores its potential
531 applicability across regions with similar climatic and morphological characteristics. Our goal is to provide a reasonable
532 assessment of vulnerability through life years lost, rather than to definitively classify flood-prone areas by societal factors.
533 Despite certain limitations, our findings offer valuable insights into regional flood risk and its key drivers.

534 With advancing technology, we can now predict the drivers of impending extreme events, enabling proactive
535 measures to mitigate their impact. Stakeholders could leverage our model to forecast vulnerability to future flood events with
536 precision, enhancing hazard assessment, decision-making, planning, and mitigation efforts.

537
538 **Competing interests:** The contact author has declared that none of the authors has any competing interests.

539 **Acknowledgment:** This work was supported by the NASA High Mountain Asia program (grant #80NSSC20K1300).

540 **Data Availability:** The FGP products are available at NASA National Snow and Ice Data Center (NSIDC)
541 (https://nsidc.org/data/hma2_fgp/versions/1)

542 **References**

543 Aksha, S. K., Juran, L., Resler, L. M., & Zhang, Y.: An Analysis of Social Vulnerability to Natural Hazards in Nepal Using
544 a Modified Social Vulnerability Index, *International Journal of Disaster Risk Science*, 10(1), 103–116.
545 <https://doi.org/10.1007/s13753-018-0192-7>, 2019.

546 Anon: China: Floods Information bulletin n° 1 GLIDE n°, [https://reliefweb.int/report/china/china-floods-information-](https://reliefweb.int/report/china/china-floods-information-bulletin-n-1-7)
547 [bulletin-n-1-7](https://reliefweb.int/report/china/china-floods-information-bulletin-n-1-7), 2010. Last accessed May 5, 2025.

548 Barlow, M., Wheeler, M., Lyon, B., and Cullen, H.: Modulation of daily precipitation over Southwest Asia by the Madden-
549 Julian oscillation, *Mon Weather Rev*, 133, 3579–3594, <https://doi.org/10.1175/MWR3026.1>, 2005.

550 Bentivoglio, R., Isufi, E., Jonkman, S. N., and Taormina, R.: Deep learning methods for flood mapping: a review of existing
551 applications and future research directions, *Hydrol Earth Syst Sci*, 26, 4345–4378, [https://doi.org/10.5194/HESS-26-4345-](https://doi.org/10.5194/HESS-26-4345-2022)
552 [2022](https://doi.org/10.5194/HESS-26-4345-2022), 2022.

553 Blench 1906-1993, T.: *Mobile-bed fluviology: a regime theory treatment of rivers for engineers and hydrologists*,
554 Edmonton (Ca.): University of Alberta press, 1969.

555 Bookhagen, B. and Burbank, D. W.: Toward a complete Himalayan hydrological budget: Spatiotemporal distribution of
556 snowmelt and rainfall and their impact on river discharge, *J Geophys Res Earth Surf*, 115,
557 <https://doi.org/10.1029/2009JF001426>, 2010.

558 Borga, M., Gaume, E., Creutin, J. D., and Marchi, L.: Surveying flash floods: Gauging the ungauged extremes, *Hydrol*
559 *Process*, 22, 3883–3885, <https://doi.org/10.1002/HYP.7111>, 2008.

560 Byers, A. C., Shugar, D. H., Chand, M. B., Portocarrero, C., Shrestha, M., Rounce, D. R., and Watanabe, T.: Three Recent
561 and Lesser-Known Glacier-Related Flood Mechanisms in High Mountain Environments, *Mt Res Dev*, 42, A12–A22,
562 <https://doi.org/10.1659/MRD-JOURNAL-D-21-00045.1>, 2022.

563 Caloiero, T., Coscarelli, R., and Gaudio, R.: Spatial and temporal variability of daily precipitation concentration in the
564 Sardinia region (Italy), *International Journal of Climatology*, 39, 5006–5021, <https://doi.org/10.1002/JOC.6123>, 2019.

565 Cavallo, E. and Noy, I.: *The Economics of Natural Disasters A Survey*, 2010.

566 Chen, T. and Guestrin, C.: XGBoost: A Scalable Tree Boosting System, *Proceedings of the ACM SIGKDD International*
567 *Conference on Knowledge Discovery and Data Mining*, 13-17-August-2016, 785–794,
568 <https://doi.org/10.1145/2939672.2939785>, 2016.

569 Chen, T., He, T., and Benesty, M.: XGBoost: eXtreme Gradient Boosting, R package version 0.71-2, 1–4, 2018.

570 Criss, R. E. and Shock, E. L.: Flood enhancement through flood control, *Geology*, 29, 875, <https://doi.org/10.1130/0091->
571 [7613\(2001\)029<0875:FETFC>2.0.CO;2](https://doi.org/10.1130/0091-7613(2001)029<0875:FETFC>2.0.CO;2), 2001.

572 Cortesi, N., Gonzalez-Hidalgo, J. C., Brunetti, M., & Martin-Vide, J.: Daily precipitation concentration across Europe 1971-
573 2010, *Natural Hazards and Earth System Science*, 12(9), 2799–2810. <https://doi.org/10.5194/nhess-12-2799-2012>, 2012.

574 Delalay, M., Ziegler, A. D., Shrestha, M. S., Wasson, R. J., Sudmeier-Rieux, K., McAdoo, B. G., & Kochhar, I.: Towards
575 improved flood disaster governance in Nepal: A case study in Sindhupalchok District, *International Journal of Disaster Risk*
576 *Reduction*, 31, 354–366. <https://doi.org/10.1016/j.ijdrr.2018.05.025>, 2018

577 Deroliya, P., Ghosh, M., Mohanty, M. P., Ghosh, S., Rao, K. H. V. D., and Karmakar, S.: A novel flood risk mapping
578 approach with machine learning considering geomorphic and socio-economic vulnerability dimensions, *Science of the Total*
579 *Environment*, 851, <https://doi.org/10.1016/j.scitotenv.2022.158002>, 2022.

580 Diehl, R. M., Gourevitch, J. D., Drago, S., and Wemple, B. C.: Improving flood hazard datasets using a low-complexity,
581 probabilistic floodplain mapping approach, *PLoS One*, 16, <https://doi.org/10.1371/journal.pone.0248683>, 2021.

582 Dingle, E. H., Creed, M. J., Sinclair, H. D., Gautam, D., Gourmelen, N., Borthwick, A. G. L., and Attal, M.: Dynamic flood
583 topographies in the Terai region of Nepal, *Earth Surf Process Landf*, 45, 3092–3102, <https://doi.org/10.1002/esp.4953>, 2020.

584 Dollan, I. J., Maina, F. Z., Kumar, S. v., Nikolopoulos, E. I., & Maggioni, V.: An assessment of gridded precipitation
585 products over High Mountain Asia, *Journal of Hydrology: Regional Studies*, 52, 101675.
586 <https://doi.org/10.1016/J.EJRH.2024.101675>, 2024.

587 Du, M., Huang, S., Leng, G., Huang, Q., Guo, Y., & Jiang, J.: Multi-timescale-based precipitation concentration dynamics
588 and their asymmetric impacts on dry and wet conditions in a changing environment, *Atmospheric Research*, 291, 106821.
589 <https://doi.org/10.1016/J.ATMOSRES.2023.106821>, 2023.

590 European Space Agency, Sinergise. Copernicus Global Digital Elevation Model: <https://doi.org/10.5069/G9028PQB>, last
591 access: 20 March 2023.

592 Fischer, M., Brettin, J., Roessner, S., Walz, A., Fort, M., and Korup, O.: Rare flood scenarios for a rapidly growing high-
593 mountain city: Pokhara, Nepal, *Natural Hazards and Earth System Sciences*, 22, 3105–3123,
594 <https://doi.org/10.5194/NHESS-22-3105-2022>, 2022.

595 Global Active Archive of Large Flood Events, Dartmouth Flood Observatory, University of Colorado, USA.:
596 <https://floodobservatory.colorado.edu/Archives/index.html>, last access: 20 March 2023.

597 Gridded Population of the World (GPW), v4 | SEDAC: <https://sedac.ciesin.columbia.edu/data/collection/gpw-v4/citations>,
598 last access: 30 April 2024.

599 Haag, I., Jones, P. D., and Samimi, C.: Central Asia’s Changing Climate: How Temperature and Precipitation Have Changed
600 across Time, Space, and Altitude, *Climate 2019*, Vol. 7, Page 123, 7, 123, <https://doi.org/10.3390/CLI7100123>, 2019.

601 Hamal, K., Sharma, S., Baniya, B., Khadka, N., and Zhou, X.: Inter-Annual Variability of Winter Precipitation Over Nepal
602 Coupled With Ocean-Atmospheric Patterns During 1987–2015, *Front Earth Sci (Lausanne)*, 8,
603 <https://doi.org/10.3389/FEART.2020.00161>, 2020.

604 Hawker, L., Rougier, J., Neal, J., Bates, P., Archer, L., and Yamazaki, D.: Implications of Simulating Global Digital
605 Elevation Models for Flood Inundation Studies, *Water Resour Res*, 54, 7910–7928, <https://doi.org/10.1029/2018WR023279>,
606 2018.

607 High Mountain Asia 8-meter DEM Mosaics Derived from Optical Imagery, Version 1 | National Snow and Ice Data Center:
608 https://nsidc.org/data/hma_dem8m_mos/versions/1, last access: 20 March 2023.

609 ICIMOD: Glacial Lakes and Glacial Lake Outburst Floods in Nepal, 2011.

610 Janizadeh, S., Kim, D., Jun, C., Bateni, S. M., Pandey, M., & Mishra, V. N.: Impact of climate change on future flood
611 susceptibility projections under shared socioeconomic pathway scenarios in South Asia using artificial intelligence
612 algorithms, *Journal of Environmental Management*, 366, 121764, <https://doi.org/10.1016/J.JENVMAN.2024.121764>, 2024.

613 Jongejan, R. B. and Maaskant, B.: Quantifying flood risks in the Netherlands, *Risk Analysis*, 35, 252–264,
614 <https://doi.org/10.1111/risa.12285>, 2015.

615 Kafle, K. R., Khanal, S. N., and Dahal, R. K.: Consequences of Koshi flood 2008 in terms of sedimentation characteristics
616 and agricultural practices, *Geoenvironmental Disasters*, 4, 1–13, <https://doi.org/10.1186/S40677-017-0069-X/FIGURES/15>,
617 2017.

618 Kansakar, S. R., Hannah, D. M., Gerrard, J., and Rees, G.: Spatial pattern in the precipitation regime in Nepal, *International
619 Journal of Climatology*, 24, 1645–1659, <https://doi.org/10.1002/JOC.1098>, 2004.

620 Karki, R., Talchabhadel, R., Aalto, J., and Baidya, S. K.: New climatic classification of Nepal, *Theor Appl Climatol*, 125,
621 799–808, <https://doi.org/10.1007/S00704-015-1549-0>, 2016.

622 Karki, R., ul Hasson, S., Schickhoff, U., Scholten, T., and Böhner, J.: Rising Precipitation Extremes across Nepal, *Climate
623 2017*, Vol. 5, Page 4, 5, 4, <https://doi.org/10.3390/CLI5010004>, 2017.

624 Kayastha, R. B. and Kayastha, R.: Glacio-Hydrological Degree-Day Model (GDM) Useful for the Himalayan River Basins,
625 Himalayan Weather and Climate and their Impact on the Environment, 379–398, [https://doi.org/10.1007/978-3-030-29684-](https://doi.org/10.1007/978-3-030-29684-1_19)
626 1_19, 2019.

627 Khanal, S., Tiwari, S., Lutz, A. F., Hurk, B. V.D., and Immerzeel, W. W.: Historical Climate Trends over High Mountain
628 Asia Derived from ERA5 Reanalysis Data, *J Appl Meteorol Climatol*, 62, 263–288, [https://doi.org/10.1175/JAMC-D-21-](https://doi.org/10.1175/JAMC-D-21-0045.1)
629 0045.1, 2023.

630 Khanam, M., Sofia, G., and Anagnostou, E. N.: To what extent do flood-inducing storm events change future flood hazards?,
631 *Hydrol. Earth Syst. Sci.*, 28, 3161–3190, <https://doi.org/10.5194/hess-28-3161-2024>, 2024.

632 Kiran S, Yogacharya, and Gautam, D. K.: Floods in Nepal: Genesis, Magnitude, Frequency and Consequences, in: Proc. of
633 the International Conference on Hydrology and Climate Change in Mountainous Areas,
634 <https://doi.org/10.13140/RG.2.1.2376.8489>, 2008.

635 Kirschbaum, D., Kapnick, S. B., Stanley, T., and Pascale, S.: Changes in Extreme Precipitation and Landslides Over High
636 Mountain Asia, *Geophys Res Lett*, 47, <https://doi.org/10.1029/2019GL085347>, 2020.

637 Lane, S. N., Tayefi, V., Reid, S. C., Yu, D., and Hardy, R. J.: Interactions between sediment delivery, channel change,
638 climate change and flood risk in a temperate upland environment, *Earth Surf Process Landf*, 32, 429–446,
639 <https://doi.org/10.1002/esp.1404>, 2007.

640 Lindersson, S., Brandimarte, L., Märd, J., and Di Baldassarre, G.: Global riverine flood risk - How do hydrogeomorphic
641 floodplain maps compare to flood hazard maps?, *Natural Hazards and Earth System Sciences*, 21, 2921–2948,
642 <https://doi.org/10.5194/nhess-21-2921-2021>, 2021.

643 Maggioni, V., & Massari, C.: On the performance of satellite precipitation products in riverine flood modeling: A review,
644 *Journal of Hydrology*, 558, 214–224. <https://doi.org/10.1016/J.JHYDROL.2018.01.039>, 2018.

645 Maina, F. Z., Kumar, S. v., Getirana, A., Forman, B., Zaitchik, B. F., Loomis, B., Maggioni, V., Xue, Y., McLarty, S., &
646 Zhou, Y.: Development of a Multidecadal Land Reanalysis over High Mountain Asia, AMS.
647 <https://ams.confex.com/ams/103ANNUAL/meetingapp.cgi/Paper/415850>, 2023.

648 Marston, R., Kleinman, J., and Miller, M.: Geomorphic and forest cover controls on monsoon flooding, central Nepal
649 Himalaya, *Mt Res Dev*, 16, 257–264, <https://doi.org/10.2307/3673948>, 1996.

650 Martin-Vide, J.: Spatial distribution of a daily precipitation concentration index in peninsular Spain, *International Journal of*
651 *Climatology*, 24, 959–971, <https://doi.org/10.1002/JOC.1030>, 2004.

652 Mathers, C., Stevens, G., Ho, J., Ma Fat, D., Retno Mahanani, W., Andreev, K., Bassani, D., Black, B., Boerma, T.,
653 Boucher, P., Bray, F., Burton, T., Campbell, H., Chou, D., Cibulskis, R., Cousens, S., Ferlay, J., Gacic-Dobo, M., Garfield,
654 R., Gemmill, A., Gerland, P., Ghys, P., Glaziou, P., Gu, D., Hill, K., Iaych, K., Inoue, M., Jakob, R., Jamison, D., Jha, P.,
655 Johnson, H., Lawn, J., Li, N., Liu, L., Lozano, R., Mahi, M., Murray, C., Newman, L., Oestergaard, M., Parkin, M., Peden,
656 M., Pelletier, F., Rehm, J., Rudan, I., Say, L., Simons, E., Sismanidis, C., Spoorenberg, T., Stannecki, K., Stover, J., Strebel,

657 P., Suzuki, E., Toroyan, T., Vos, T., Wardlaw, T., White, R., Wilmoth, J., and You, D.: WHO methods and data sources for
658 global burden of disease estimates 2000-2011, 2013.

659 Manfreda S and Samela C.: A digital elevation model based method for a rapid estimation of flood inundation depth, Journal
660 of Flood Risk Management, <https://doi.org/10.1111/jfr3.1254110>, 2019.

661 Mazzoleni, M., Dottori, F., Cloke, H. L., and Di Baldassarre, G.: Deciphering human influence on annual maximum flood
662 extent at the global level, *Commun Earth Environ*, 3, <https://doi.org/10.1038/s43247-022-00598-0>, 2022.

663 Meyer, V., Becker, N., Markantonis, V., Schwarze, R., Van Den Bergh, J. C. J. M., Bouwer, L. M., Bubeck, P., Ciavola, P.,
664 Genovese, E., Green, C., Hallegatte, S., Kreibich, H., Lequeux, Q., Logar, I., Papyrakis, E., Pfuertscheller, C., Poussin, J.,
665 Przulski, V., Thielen, A. H., and Viavattene, C.: Review article: Assessing the costs of natural hazards-state of the art and
666 knowledge gaps, <https://doi.org/10.5194/nhess-13-1351-2013>, 2013.

667 Miles, E., McCarthy, M., Dehecq, A., Kneib, M., Fugger, S., & Pellicciotti, F.: Health and sustainability of glaciers in High
668 Mountain Asia, *Nature Communications* 2021 12:1, 12(1), 1–10. <https://doi.org/10.1038/s41467-021-23073-4>, 2021.

669 Mohanty, M. P. and Simonovic, S. P.: A Comprehensive Approach for Floodplain Mapping through Identification of Hazard
670 Using Publicly Available Data Sets over Canada, *Water (Switzerland)*, 14, <https://doi.org/10.3390/w14142280>, 2022.

671 Monjo, R. and Martin-Vide, J.: Daily precipitation concentration around the world according to several indices, *International*
672 *Journal of Climatology*, 36, 3828–3838, <https://doi.org/10.1002/JOC.4596>, 2016.

673 Monjo, R.: Measure of rainfall time structure using the dimensionless n-index, *Clim Res*, 67, 71–86,
674 <https://doi.org/10.3354/cr01359>, 2016.

675 Mosavi, A., Ozturk, P., and Chau, K. W.: Flood prediction using machine learning models: Literature review,
676 <https://doi.org/10.3390/w10111536>, 27 October 2018.

677 Nepal - Floods and Landslides Jul 1993 UN DHA Situation Reports 1-8 - Nepal | ReliefWeb:
678 <https://reliefweb.int/report/nepal/nepal-floods-and-landslides-jul-1993-un-dha-situation-reports-1-8>, last access: 6 February
679 2023.

680 Nepal - Floods Situation Report No. 1, 26 July 1996 - Nepal | ReliefWeb: <https://reliefweb.int/report/nepal/nepal-floods-situation-report-no-1-26-july-1996>, last access: 6 February 2023.

681 Nepal Appeal No. 01.55/2003 Annual Report - Nepal | ReliefWeb: <https://reliefweb.int/report/nepal/nepal-appeal-no-01552003-annual-report>, last access: 6 February 2023.

682 Nepal: Landslides and Floods - Aug 2014 | ReliefWeb: <https://reliefweb.int/disaster/ls-2014-000103-npl>, last access: 6
685 February 2023.

686 Neuhold, C., Stanzel, P., and Nachtnebel, H. P.: Incorporating river morphological changes to flood risk assessment:
687 Uncertainties, methodology and application, *Natural Hazards and Earth System Science*, 9, 789–799,
688 <https://doi.org/10.5194/nhess-9-789-2009>, 2009.

689 Noy, I.: A Global Comprehensive Measure of the Impact of Natural Hazards and Disasters, *Glob Policy*, 7, 56–65,
690 <https://doi.org/10.1111/1758-5899.12272>, 2016a.

691 Noy, I.: Comparing the direct human impact of natural disasters for two cases in 2011: The Christchurch earthquake and the
692 Bangkok flood, *International Journal of Disaster Risk Reduction*, 13, 61–65, <https://doi.org/10.1016/j.ijdr.2015.03.009>,
693 2015.

694 Noy, I.: Natural disasters in the Pacific Island Countries: new measurements of impacts, *Natural Hazards*, 84, 7–18,
695 <https://doi.org/10.1007/s11069-015-1957-6>, 2016b.

696 Noy, I.: Prepared for the 2015 Global Assessment Report on Disaster Risk Reduction A Non-Monetary Global Measure Of
697 the Direct Impact of Natural Disasters, 2014.

698 Pangali Sharma, T. P., Zhang, J., Koju, U. A., Zhang, S., Bai, Y., and Suwal, M. K.: Review of flood disaster studies in
699 Nepal: A remote sensing perspective, <https://doi.org/10.1016/j.ijdr.2018.11.022>, 1 March 2019.

700 Pervin, I. A., Rahman, S. M. M., Nepal, M., Haque, A. K. E., Karim, H., and Dhakal, G.: Adapting to urban flooding: A case
701 of two cities in South Asia, *Water Policy*, 22, 162–188, <https://doi.org/10.2166/wp.2019.174>, 2020.

702 Piacentini, T., Carabella, C., Boccabella, F., Ferrante, S., Gregori, C., Mancinelli, V., Pacione, A., Pagliani, T., and
703 Miccadei, E.: Geomorphology-Based analysis of flood critical areas in small hilly catchments for civil protection purposes
704 and earlywarning systems: The case of the feltrino stream and the Lanciano Urban Area (Abruzzo, Central Italy), *Water*
705 (Switzerland), 12, <https://doi.org/10.3390/w12082228>, 2020.

706 Pinter, N., Jemberie, A. A., Remo, J. W. F., Heine, R. A., and Ickes, B. S.: Flood trends and river engineering on the
707 Mississippi River system, *Geophys. Res. Lett*, 35, 23404, <https://doi.org/10.1029/2008GL035987>, 2008.

708 Rentschler, J., Salhab, M., and Jafino, B. A.: Flood exposure and poverty in 188 countries, *Nat Commun*, 13,
709 <https://doi.org/10.1038/s41467-022-30727-4>, 2022.

710 Saki, S. A., Sofia, G., and Anagnostou, E. N.: Characterizing CONUS-wide spatio-temporal changes in daily precipitation,
711 flow, and variability of extremes, *J Hydrol (Amst)*, 626, 130336, <https://doi.org/10.1016/J.JHYDROL.2023.130336>, 2023.

712 Samela, C., Troy, T. J., and Manfreda, S.: Geomorphic classifiers for flood-prone areas delineation for data-scarce
713 environments, *Adv Water Resour*, 102, 13–28, <https://doi.org/10.1016/j.advwatres.2017.01.007>, 2017.

714 Sangüesa, C., Pizarro, R., Ibañez, A., Pino, J., Rivera, D., García-Chevesich, P., and Ingram, B.: Spatial and temporal
715 analysis of rainfall concentration using the Gini Index and PCI, *Water (Switzerland)*, 10, <https://doi.org/10.3390/w10020112>,
716 2018.

717 Sanyal, J. and Lu, X. X.: Application of Remote Sensing in Flood Management with Special Reference to Monsoon Asia: A
718 Review, *Natural Hazards*, 283–301 pp., 2004.

719 Serrano-Notivoli, R., Martín-Vide, J., Saz, M. A., Longares, L. A., Beguería, S., Sarricolea, P., Meseguer-Ruiz, O., and de
720 Luis, M.: Spatio-temporal variability of daily precipitation concentration in Spain based on a high-resolution gridded data
721 set, *International Journal of Climatology*, 38, e518–e530, <https://doi.org/10.1002/JOC.5387>, 2018.

722 Shamsudduha, M. and Panda, D. K.: Spatio-temporal changes in terrestrial water storage in the Himalayan river basins and
723 risks to water security in the region: A review, *International Journal of Disaster Risk Reduction*, 35,
724 <https://doi.org/10.1016/J.IJDRR.2019.101068>, 2019.

725 Sharma, P. p. T., Zhang, J., Koju, A. U., Zhang, S., Bai, Y., and Suwal, K. M.: International Journal of Disaster Risk
726 Reduction Review of flood disaster studies in Nepal : A remote sensing perspective Til Prasad Pangali Sharma, International
727 Journal of Disaster Risk Reduction, 34, 18–27, 2019.

728 Shean, D.: High Mountain Asia 8-meter DEM Mosaics Derived from Optical Imagery, Version 1 | National Snow and Ice
729 Data Center, https://nsidc.org/data/hma_dem8m_mos/versions/1, 2017.

730 Shrestha, A. B. and Aryal, R.: Climate change in Nepal and its impact on Himalayan glaciers, Reg Environ Change, 11, 65–
731 77, <https://doi.org/10.1007/s10113-010-0174-9>, 2011.

732 Shrestha, A. B., Eriksson, M., Mool, P., Ghimire, P., Mishra, B., and Khanal, N. R.: Glacial lake outburst flood risk
733 assessment of Sun Koshi basin, Nepal, Geomatics, Natural Hazards and Risk, 1, 157–169,
734 <https://doi.org/10.1080/19475701003668968>, 2010.

735 Simonovic, S. P., Karmakar, S., Cheng, Z., Kansal, M. L., and Singh, S.: Flood Management Issues in Hilly Regions of
736 Uttarakhand (India) under Changing Climatic Conditions, Water 2022, Vol. 14, Page 1879, 14, 1879,
737 <https://doi.org/10.3390/W14121879>, 2022.

738 Slater, L. J., Singer, M. B., and Kirchner, J. W.: Hydrologic versus geomorphic drivers of trends in flood hazard, Geophys
739 Res Lett, 42, 370–376, <https://doi.org/10.1002/2014GL062482>, 2015.

740 Sofia, G. and Nikolopoulos, E. I.: Floods and rivers: a circular causality perspective, Sci Rep, 10,
741 <https://doi.org/10.1038/s41598-020-61533-x>, 2020a.

742 Sofia, G.: Combining geomorphometry, feature extraction techniques and Earth-surface processes research: The way
743 forward, Geomorphology (Vol. 355, p. 107055), Elsevier B.V. <https://doi.org/10.1016/j.geomorph.2020.107055>, 2020b.

744 Sofia, G., Ragazzi, F., Giandon, P., Dalla Fontana, G., and Tarolli, P.: On the linkage between runoff generation, land
745 drainage, soil properties, and temporal patterns of precipitation in agricultural floodplains, Adv Water Resour, 124, 120–138,
746 <https://doi.org/10.1016/j.advwatres.2018.12.003>, 2019.

747 Sofia, G., Di Stefano, C., Ferro, V., and Tarolli, P.: Morphological Similarity of Channels: From Linear Erosional Features
748 (Rill, Gully) to Alpine Rivers, Land Degrad Dev, 28, 1717–1728, <https://doi.org/10.1002/ldr.2703>, 2017.

749 Sofia, G., Tarolli, P., Cazorzi, F., and Dalla Fontana, G.: Downstream hydraulic geometry relationships: Gathering reference
750 reach-scale width values from LiDAR, Geomorphology, 250, 236–248, <https://doi.org/10.1016/j.geomorph.2015.09.002>,
751 2015.

752 Stover, S. C. and Montgomery, D. R.: Channel change and flooding, Skokomish River, Washington, J Hydrol (Amst), 243,
753 272–286, [https://doi.org/10.1016/S0022-1694\(00\)00421-2](https://doi.org/10.1016/S0022-1694(00)00421-2), 2001.

754 Subba, S., Ma, Y., and Ma, W.: Spatial and Temporal Analysis of Precipitation Extremities of Eastern Nepal in the Last Two
755 Decades (1997–2016), Journal of Geophysical Research: Atmospheres, 124, 7523–7539,
756 <https://doi.org/10.1029/2019JD030639>, 2019.

757 Talchabhadel, R., Karki, R., Thapa, B. R., Maharjan, M., and Parajuli, B.: Spatio-temporal variability of extreme
758 precipitation in Nepal, International Journal of Climatology, 38, 4296–4313, <https://doi.org/10.1002/JOC.5669>, 2018.

759 Torti, J. M. I.: Floods in Southeast Asia: A health priority, *J Glob Health*, 2, <https://doi.org/10.7189/jogh.02.020304>, 2012.

760 Tuladhar, D., Dewan, A., Kuhn, M., and Corner, R. J.: Spatio-temporal rainfall variability in the Himalayan mountain
761 catchment of the Bagmati River in Nepal., *Theor Appl Climatol*, 139, 599–615, [https://doi.org/10.1007/S00704-019-02985-](https://doi.org/10.1007/S00704-019-02985-8)
762 8, 2020.

763 WHO: GlobalDALYmethodsJapan_2011_WHO, World Health Organization, 4, 2014.

764 Winiger, M., Gumpert, M., and Yamout, H.: Karakorum-Hindukush-western Himalaya: Assessing high-altitude water
765 resources, *Hydrol Process*, 19, 2329–2338, <https://doi.org/10.1002/HYP.5887>, 2005.

766 World Bank, 2012. Weather and Climate Services in Europe and Central Asia: A Regional Review.

767 Yang, C. R. and Tsai, C. T.: Development of a GIS-based flood information system for floodplain modeling and damage
768 calculation, *J Am Water Resour Assoc*, 36, 567–577, <https://doi.org/10.1111/j.1752-1688.2000.tb04287.x>, 2000.

769 Zheng, G., Allen, S. K., Bao, A., Ballesteros-Cánovas, J. A., Huss, M., Zhang, G., Li, J., Yuan, Y., Jiang, L., Yu, T., Chen,
770 W., and Stoffel, M.: Increasing risk of glacial lake outburst floods from future Third Pole deglaciation, *Nat Clim Chang*, 11,
771 411–417, <https://doi.org/10.1038/s41558-021-01028-3>, 2021.

772 Zheng, X., Maidment, D. R., Tarboton, D. G., Liu, Y. Y., and Passalacqua, P.: GeoFlood: Large-Scale Flood Inundation
773 Mapping Based on High-Resolution Terrain Analysis, *Water Resour Res*, 54, 10,013-10,033,
774 <https://doi.org/10.1029/2018WR023457>, 2018.